

THESIS / THÈSE

DOCTOR OF SCIENCES

Selective growth of CdTe by molecular beam epitaxy on CdTe(211)B microseeds and Si(100) nanoseeds patterned on SiO₂

Seldrum, Thomas

Award date:
2009

Awarding institution:
University of Namur

[Link to publication](#)

General rights

Copyright and moral rights for the publications made accessible in the public portal are retained by the authors and/or other copyright owners and it is a condition of accessing publications that users recognise and abide by the legal requirements associated with these rights.

- Users may download and print one copy of any publication from the public portal for the purpose of private study or research.
- You may not further distribute the material or use it for any profit-making activity or commercial gain
- You may freely distribute the URL identifying the publication in the public portal ?

Take down policy

If you believe that this document breaches copyright please contact us providing details, and we will remove access to the work immediately and investigate your claim.

Chapter V. Experimental Results and
Discussion

The aim of this PhD thesis is to demonstrate that it is possible to achieve selective growth of II-VI compounds by molecular beam epitaxy and to explain why it is possible.

The first part of the presented experimental results consists of the cleaning procedure to obtain a high quality Si substrate. Although the CdTe layer is usually grown on Si(211), the Si(111) orientation is studied to analyze the cleaning processes because this orientation is more suitable for scanning tunneling microscopy and low energy electron diffraction characterizations. In addition, Si(211) is mostly made of Si(111) terraces, hence the results obtained on the (111) face can easily be transposed to the (211) face.

For the same reason, the second part of the silicon preparation consisting of the arsenic passivation is also studied on the (111) face. It is demonstrated that the preparation of the initial substrate (passivated silicon) is well controlled and suitable for subsequent growth of ZnTe and CdTe layers.

The third part presents the growth technique used to produce thick layer of CdTe(211)B/ZnTe(211)B/As/Si(211) by molecular beam epitaxy with the OPUS 45 system. The layer is characterized by reflection of high energy electron diffraction, X-ray diffraction and double crystal rocking curve.

The fourth section deals with the temperature calibration of the MBE system of the LPEM and the study of the growth rate of CdTe for different substrate temperatures.

The next sections concern the selective growth of CdTe on two different kinds of samples: the first consists of CdTe(211)B seeds on SiO₂ and the second is Si(100) seeds on SiO₂. The difference in the two experiments is the chemical nature of the seeds and the size of the seeds (micron scale and nanometer scale respectively). Sections 5 and 6 concern the first study of selective growth. A CdTe layer is patterned by optical lithography to produce the desired islands of CdTe on Si. The lithography process is explained and the patterned structures are analyzed using scanning, Auger and photoemission electron microscopies and profilometry. Selective growth of CdTe on such patterned CdTe seeds on Si (oxidized by exposure to air) is successfully performed in the LPEM MBE system and the result is studied by photoemission electron microscopy and profilometry.

The second experiment on selective growth is carried out on SOI (silicon on insulator) samples patterned by interferometric lithography (section 7). This mode of lithography is briefly explained and the results of the patterning at the nanometer scale are analyzed by SEM and AFM. The eighth part is dedicated to the selective growth of CdTe on Si seeds in the OPUS 45 system. The feasibility of selective growth on this substrate is demonstrated by SEM, AFM and XPS experiments.

The last part (section 9) deals with the selective growth mechanism. It is explained by considering a difference in the physisorption energies of CdTe on Si, SiO₂ and CdTe.

V.1. Silicon cleaning and characterization

Both in-situ and ex-situ cleaning procedures are possible routes to obtain a pure Si surface. Both techniques have been studied on Si(111) and the results are characterized by LEED, AES and STM.

V.1.A. In-situ cleaning

The in-situ cleaning is carried out in the UHV environment with a base pressure of $1 \cdot 10^{-10}$ mbar. A Si(111) loaded in the UHV system is mounted on an isolated stage provided by Omicron Nanotechnology. The untreated Si(111) surface consists of a Si single crystal covered by a native oxide on the surface. A layer of organic and inorganic contaminants is present on the sample surface because of air exposure for an extended period of time.

Three experimental facilities can be used at the LPEM to check the efficiency of the in-situ chemical cleaning: low energy electron diffraction (LEED) characterizing the cristallinity, Auger electron spectroscopy (AES) for the chemical purity and scanning tunneling microscopy (STM) to analyze the topography of the surface.

Auger electron spectroscopy (AES) shows the signature of the chemical species present at the surface of the untreated silicon sample (Figure V-1, black curve). The presence of Si (in its oxidized form), O and C are detected. The kinetic energy of the Auger electrons related to these chemical elements is presented in Table V-1. Reference values are found in [70].

For in-situ cleaning, the sample is first progressively outgassed up to 200°C for 8 hours. This annealing is achieved by passing a current directly through the sample (direct heating technique). During this step, the pressure in the chamber rises up to $1 \cdot 10^{-9}$ mbar.

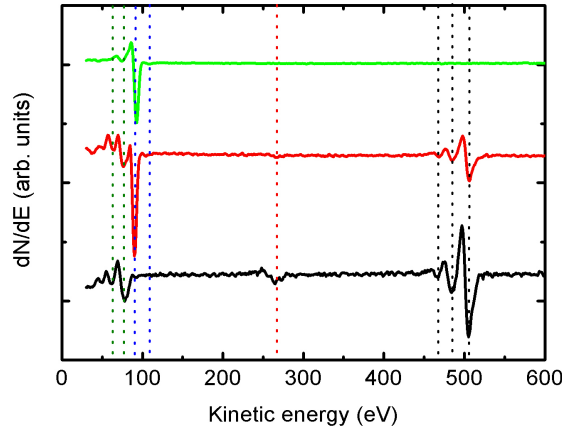


Figure V-1. AES spectra of untreated silicon (black), after Ar^+ sputtering (red) and after annealing at 900°C (green). The dotted lines are referred in Table V-1.

Chemical element	Kinetic energy (eV) from [70]	Measured kinetic energy (eV)
Si_{LMM} (oxidized)	76	78 ± 2
	59 and 63	62 ± 2
Si_{LMM} (metallic)	92	93 ± 2
	107	109 ± 2
C_{KLL}	272	270 ± 2
O_{KLL}	468	468 ± 2
	483	484 ± 2
	503	505 ± 2

Table V-1. Kinetic energies of Si_{LMM} , C_{KLL} and O_{KLL} observed in Figure V-1.

The second step of the treatment consists of an ionic sputtering of the sample. The Si(111) is sputtered for 2 minutes by Ar^+ ions produced by a cold cathode ion gun. The energy of the ions is 1 keV and a pressure of $7.0 \cdot 10^{-6}$ mbar is introduced in the UHV chamber, producing a readout ion current of about 30 μA . This current is a measure of the collected ions integrated on the entire surface of the heating stage holding the silicon sample holder. After sputtering, the silicon sample is heated up to 300°C by direct heating to desorb the Ar atoms implanted in the matrix after the sputtering. AES demonstrates that only oxidized Si and O are still present at the surface (Figure V-1, red curve). At this step, the low energy electron diffraction (LEED) pattern is blurred because of the disorder created at the surface by the sputtering and due to the presence of the amorphous structure of SiO_2 .

The last step consists of heating the sputtered surface up to 1050°C to desorb the SiO₂ covering layer and to reconstruct the surface. This high temperature is reached step by step: the sample is first heated up to 500°C, defined as the standby temperature. The sample is then progressively heated up to 1050°C. If the pressure rises beyond 1.0 10⁻⁹ mbar during the procedure, the sample is set back to the standby temperature. When the pressure is low enough, the heating process starts again. Once the sample temperature reaches 1050°C with a chamber pressure below 1.0 10⁻⁹ mbar, the cooling process starts. The sample temperature decreases from 1050°C to room temperature in about 20 minutes. This slow cooling process enhances the surface reconstruction. As shown on Figure V-1 (green curve), only Si is detected on the AES spectrum. The LEED pattern shows the 7x7 reconstruction and atomic resolution can be achieved by STM (not shown here).

Even if this in-situ process leads to a perfect Si(111) 7x7 surface, it is only suitable for very small substrates. Indeed, a homogenous Ar⁺ sputtering is hardly achievable on larger substrates and the problem is that nowadays the silicon wafers used in the semiconductor industry have a diameter of 3, 4 or 5 inches (even more). The ex-situ cleaning described hereafter is suitable for larger substrates.

V.1.B. Ex-situ cleaning

V.1.B.1. RCA cleaning process

The ex-situ process consists of a wet chemical cleaning, called RCA process. This procedure has been developed by Kern *et al.* in the '70 in the RCA Laboratories [41, 71] and is still widely used to clean large silicon wafers in the semiconductor industry. The original RCA process consists of 4 steps in a row, with de-ionized water (DI) rinsing between each step and drying the wafer by spinning at the end (Figure V-2). The four active steps remove the particles and the organic and metallic contaminants from the surface and etch the oxide layer of silicon.

The results presented in this thesis concern a modified RCA process. The reason of this modification is that several steps of the initial process are redundant. This modified process requires less steps and the steps are performed in a different way (Figure V-3). The effects of the cleaning steps are based on chemical reactions and reduction-oxidation processes.

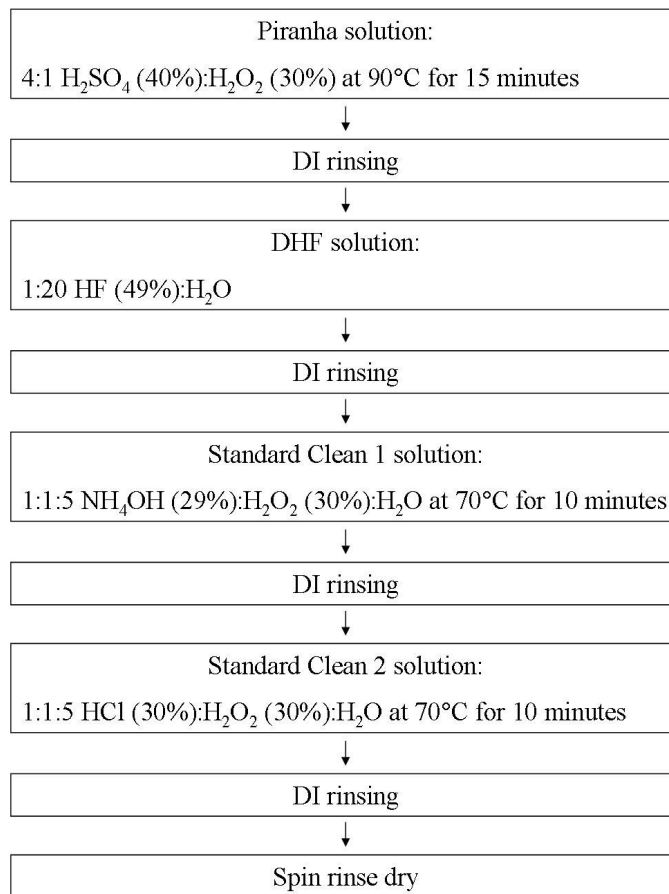


Figure V-2. RCA process by Kern *et al.* [41].

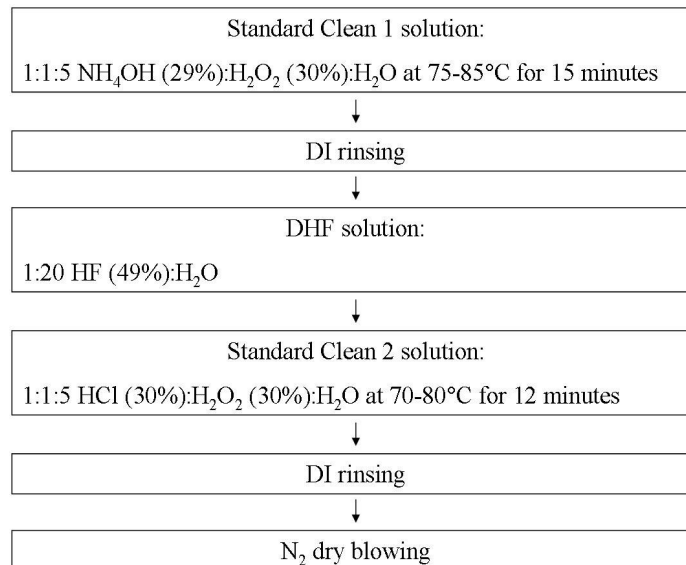


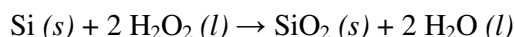
Figure V-3. Modified RCA process.

In the Standard Clean 1 solution, ammonium hydroxide (NH₄OH) and hydrogen peroxide (H₂O₂) have four cleaning effects:

- When the wafer is dipped in the solution, the OH⁻ ions react both with the wafer and the adsorbed particles. The result is that both the particles and the wafer become negatively charged. Because of Coulomb electrostatic forces, these charges repel each other;
- Chemical reactions between the solution and the wafer occur. The ammonium hydroxide reacts with the SiO₂. Hence it acts as an etchant:



The hydrogen peroxide gives its extra oxygen to the silicon substrate and creates a thin oxide film:

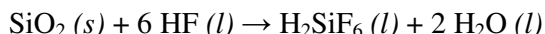


These two steps contribute to create and remove permanently an oxide layer on the surface. The creation of the oxide lifts the particles and when the oxide is removed, the particles are separated from the wafer;

- Organic impurities are mainly carbon and/or hydrogen based. Hydrogen peroxide reacts with carbon-based compounds and readily produces CO₂ (g) and H₂O (l);
- Ammonia complexes many metallic ions (Au, Ag, Cu, Ni...). This can remove metal traces present at the surface of the sample.

At the end of the standard clean 1 step, an organic contaminant free surface covered by a thin oxide layer is obtained.

The diluted HF solution (DHF) is then used to etch the oxide remaining at the end of the previous step:

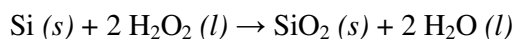


A pure Si surface is obtained at the end of this second cleaning step. With HF solution diluted with DI to obtain a 2% HF solution, a dipping time of 30 seconds is long enough to remove the oxide layer. The etching rate using HF increases if the temperature or the concentration of the solution increases.

The last chemical solution (standard clean 2) has two effects:

- Cl⁻ ions react with metallic ions of the surface to carry it away. The metallic species attacked by the chloride ions are Al³⁺, Fe³⁺, Mg³⁺ ...;

- The hydrogen peroxide reacts with the bare Si to form a clean and thin oxide layer of SiO₂ of about 1 nm:



At the end of this cleaning step, a pure silicon substrate covered by a contaminant free oxide layer is obtained.

After the standard clean 1 and 2 steps, the wafer is rinsed in 6 successive beakers of DI water.

The effects of this rinsing are of two kinds:

- DI water dissolves chemicals and reaction products;
- The rinsing may also be used to stop the action of chemical agents involved in the cleaning procedure.

After the last rinsing beaker, the Si sample is blown dry with nitrogen, mounted on a molybdenum sample holder and quickly introduced in the load-lock of the UHV system to avoid any contamination.

This oxide layer is desorbed in UHV environment by heating the substrate up to 1050°C by direct heating.

V.1.B.2. Ex-situ cleaning characterization

In the previous section, it is demonstrated that the in-situ Ar⁺ sputtering cleaning technique leads to silicon substrates of high crystalline quality and purity. In this section, a Si(111) sample is cleaned according to the modified RCA process. An untreated sample is also analyzed as a reference.

The AES results are presented in Figure V-4. The oxide is removed by heating the substrate up to 1050°C by direct heating (transition from the red to the green curve).

The different peaks observed in the Figure V-4a are referenced in Table V-2. A detailed scan around the Si_{LMM}, C_{KLL} and O_{KLL} regions are respectively presented in Figure V-4b, c and d.

On the reference sample (black curves), the oxide is so thick that only the signature of the LMM transition in Si under the oxidized form can be seen in the AES spectrum. The C_{KLL}

peak is also detected because of numerous organic contaminants on the top surface of the sample.

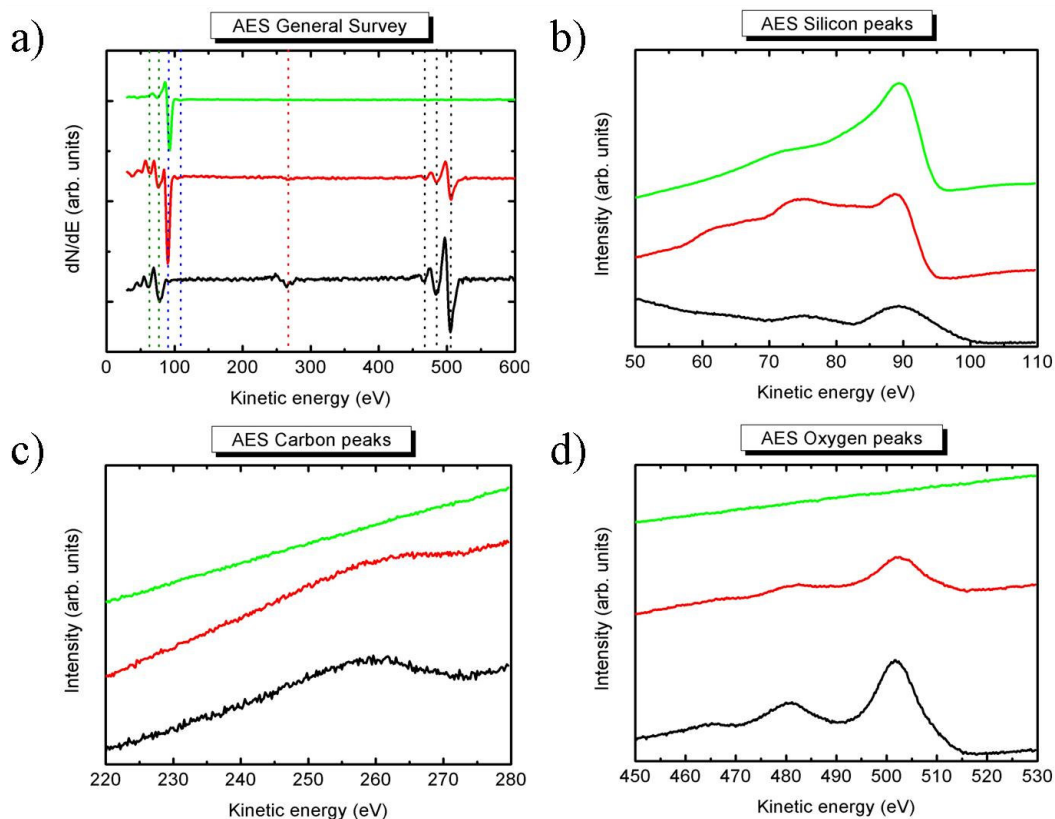


Figure V-4. AES spectra of Si(111): reference (black), RCA cleaned Si(111) before (red) and after (green) oxide removal. a) General survey; b) Si_{LMM} peaks; c) C_{KLL} peaks and d) O_{KLL} peaks.

Chemical element	Kinetic energy (eV) from [70]	Measured kinetic energy (eV)
Si_{LMM} (oxidized)	76	77 ± 1.7
	59 and 63	63 ± 1.7
Si_{LMM} (metallic)	92	92 ± 1.7
	107	107 ± 1.7
C_{KLL}	272	267 ± 1.7
O_{KLL}	468	467 ± 1.7
	483	485 ± 1.7
	503	505 ± 1.7

Table V-2. Kinetic energies of Si_{LMM} , C_{KLL} and O_{KLL} observed in Figure V-4.

Before the oxide removal (red curves), the RCA cleaned Si(111) is contaminated by carbon because of the small time interval between the end of the cleaning procedure and the loading in the UHV environment. It is easily seen from the Si region that both pure and oxidized silicon peaks are detected. This is explained by the fact that the AES technique probed about

3λ below the sample surface, where λ is the mean free path of the electrons. For electrons with an emerging kinetic energy of about 100 eV, it is found that $\lambda \approx 0.6$ nm (Figure III-3). So, 3λ is more than the expected thickness of SiO_2 of 1 nm obtained at the end of the RCA process.

The efficiency of the modified RCA method is evidenced after the oxide removal by heating the sample up to 1050°C (green curves): a pure, C-free Si surface is observed.

To ensure a high crystalline quality of the silicon substrate, the wafer is heated up to 1200°C after the oxide removal. The cooling process after the oxide desorption is of primary importance. The cooling has to be slow enough to allow an atomic reconstruction on the surface to decrease the number of highly reactive dangling bonds created by the oxide removal. LEED is used to monitor the surface crystallinity after the cooling process. For Si(111), a 7×7 reconstruction is obtained [72]. Figure V-5 presents the LEED diffraction pattern of a highly crystalline Si(111) 7×7 surface. The incident beam for this picture is characterized by an energy of 43.7 eV. The spots are well defined and the background is low. From equations (3.19) and (3.20), the lattice parameter can be calculated:

$$a_{\text{Si}(111)} \text{ (nm)} = 0.376 \pm 0.01$$

This result is the mean value of three measures done at 3 different energies. The error corresponds to the standard deviation calculated from the mean value and the three experimental results. Based on the theoretical value of $a_{\text{Si}(111)}^{\text{th}} = \frac{a_{\text{Si}(100)} \cdot \sqrt{2}}{2} = 0.384$ nm, a relative error of 2% is calculated.

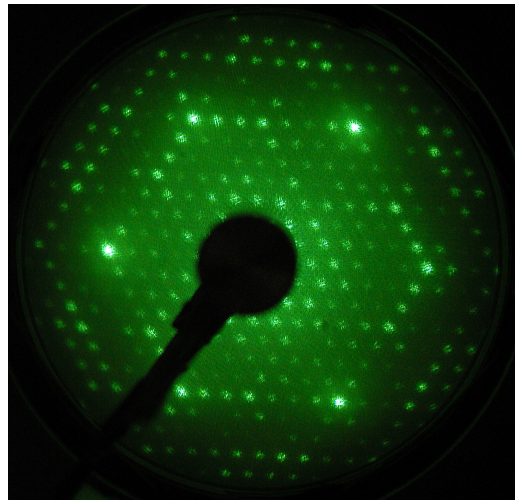


Figure V-5. LEED pattern of Si(111) 7×7 at an energy of 43.7 eV.

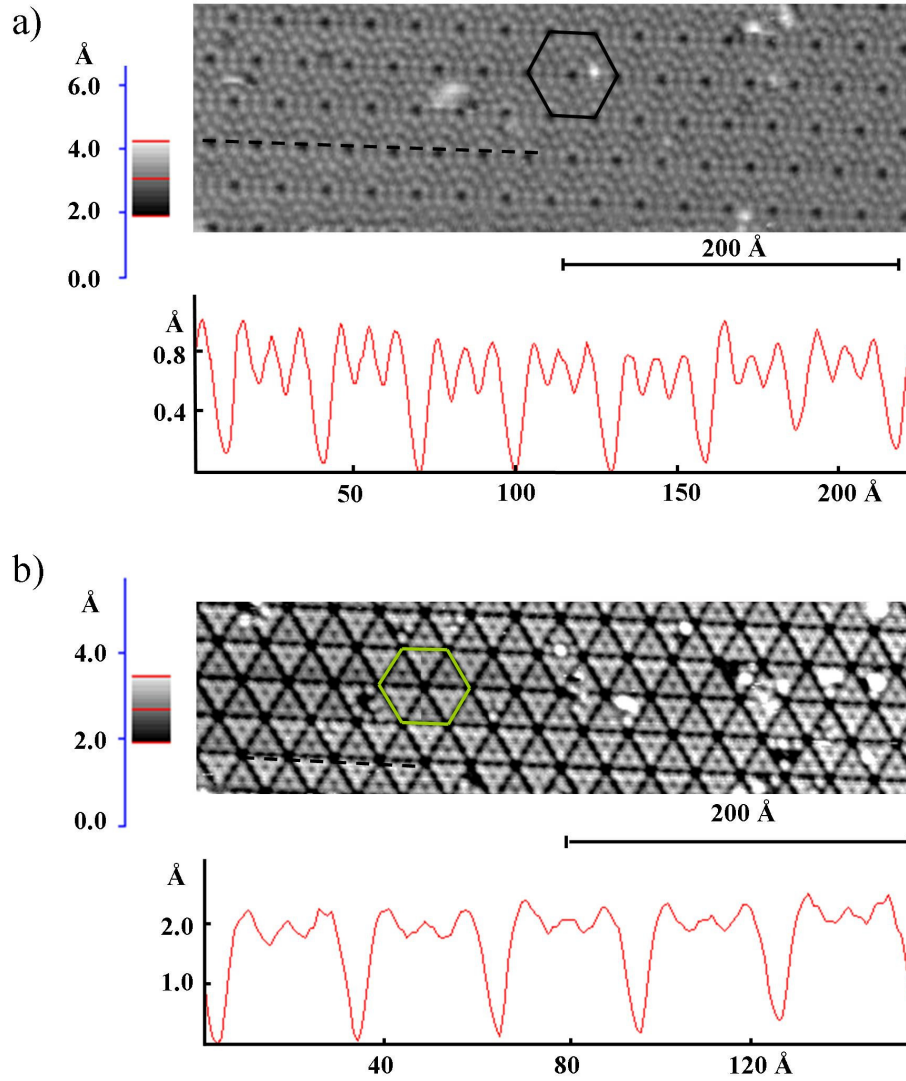


Figure V-6. STM pictures of Si(111) 7x7. a) $I = 0.4$ nA and $V = 1.5$ V; b) $I = 0.25$ nA and $V = -2.0$ V.

When the cooling of the sample is optimized, atomic resolution can be achieved by STM and the result is a surface with a very low defect density (Figure V-6). The image presented are drift corrected: assuming that the drift is negligible in the direction of the scanning direction, the distance between two adjacent holes is 26.9 \AA . To correct the drift in the direction perpendicular to the scanning direction, the horizontal lines parallel to the scanning direction of a hexagonal unit cell are shifted so that the atoms of the opposite edges perfectly face each other or in other words that the hexagon is not distorted. The width and the height of the cell are then adjusted to observe angles of 120° between all the adjacent sides of the hexagon. In Figure V-6a, the sample is positively polarized, leading to the imaging of the empty states of Si(111). In Figure V-6b, the filled states of the sample are probed because the bias between the sample and the tip is negative. Line profiles are presented to show the high resolution of

the STM pictures. The observed (7x7) reconstruction is known for a long time, and theoretical and experimental studies have been carried out to explain it [73-79]. This reconstruction exists to decrease the surface free energy: the silicon atoms have a tetrahedral coordination, with binding sp^3 orbitals. At the interface between silicon and vacuum, the last Si layer contains atoms with one dangling bond perpendicular to the surface. When the substrate temperature is high enough to initiate the reconstruction mechanism, the atoms of the top surface rearrange each other to minimize the dangling bonds density, resulting in the well-known 7x7 reconstruction. Indeed, a 7x7 unreconstructed unit cell contains 49 dangling bonds whereas the reconstruction presented in Figure V-7 presents only 19 dangling bonds: 12 for the adatoms, 6 for the rest atoms and 1 at the center atom deep in the corner hole. The DAS model explains the 7x7 reconstruction: the unit cell can be split in two triangles, one faulted (on the left) and one unfaulted (on the right). Dimers are created along the triangular area and a vacancy is present at the corner of each 7x7 unit cell. In the faulted region, the adatoms of the top layer are at a height slightly different from the adatoms of the unfaulted region because of the stacking difference. With a negative sample bias, the contrast observed in the STM picture is explained by the height difference between the faulted and the unfaulted regions and because of the coordination difference between a rest atom and an adatom [80].

In conclusion, it is demonstrated that the modified RCA process leads to the production of a clean, flat and reconstructed Si(111) 7x7 surface. The same cleaning process can be performed on Si(211) to prepare the substrate for the subsequent growth of CdTe.

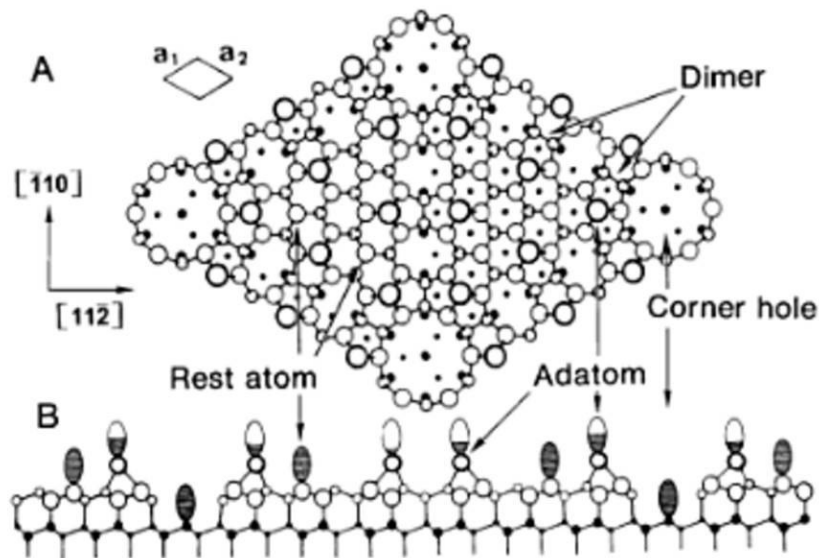


Figure V-7. DAS model of Si(111) 7x7: a) Top view and b) side view [81]. The electronic density of the rest atoms, the adatoms and the corner holes are presented in b).

V.2. As/Si(111) characterization

For the growth of CdTe, the second step after the oxide removal consists of cooling the silicon from high temperature (1200°C) to about 400°C under a flux of As₄. The As passivation of the silicon substrate ensures the B polarity of the subsequent CdTe growth. This Te terminated face is the only one suitable for further growth of HgCdTe on top of the CdTe layer.

The efficiency of the passivation process is studied on a Si(111) substrate. The flatness of this surface is convenient for STM analysis after the As passivation.

The sample is cleaned following the modified RCA process detailed in section V.1.B.2. It is then mounted on molybdenum sample holder suitable for direct heating and loaded in the UHV environment. The sample is outgassed for 10 hours in a preparation chamber at about 330°C to remove adsorbed C-based contaminant. The sample is then transferred in the liquid nitrogen cooled LPEM MBE chamber and heated up to 1200°C by direct heating. The oxide desorption is observed by reflection of high energy electron diffraction (RHEED). During the heating of the substrate, an As₄ evaporation cell is heated to 250°C. Just before the oxide desorption, the shutter of the As₄ cell is opened to expose the Si(111) to the passivation flux. The sample is cooled down to 330°C in 20 minutes. When the substrate temperature reaches 400°C, the As₄ flux is interrupted by closing the shutter and the cell temperature is set to 50°C.

The sample is then transferred back to the preparation chamber to cool it down to room temperature. This sample is characterized by STM and LEED to observe the passivation of Si(111) with arsenic.

V.2.A. STM characterization

The STM image is presented at Figure V-8. The bright regions are associated with the localization of As atoms. The initial 7x7 reconstruction is no more visible: after the arsenic passivation, a 1x1 symmetry is observed. Detailed study [82] demonstrated that after the As deposition, a relaxation of the surface occurs: the bond between a silicon and an arsenic atom is 0.242 nm, compared to bulk silicon and arsenic bonds of respectively 0.235 and 0.255 nm.

The lattice parameter measured on the STM picture is 3.8 Å, which corresponds to the in-plane lattice parameter of Si(111). This pseudomorphic growth of As on Si(111) is due to the fact that only 1 ML of As is deposited on the substrate during the cooling process [83]. To understand the contrast of the picture, it is necessary to describe the surface electronic structure. The As atoms substitute the Si atoms of the first top layer [84, 85]. Because of the higher valency of the As atoms, the dangling-bond states existing on a Si terminated surface are replaced by doubly occupied As lone-pair states. The 7x7 reconstruction was explained by the tendency to decrease the number of dangling bonds. Due to the arsenic passivation, the dangling bond reduction is no longer a driving force for reconstruction, resulting in a 1x1 surface. Moreover, the lone-pair state of the arsenic creates an occupied resonant surface state [86, 87] characterized by a p_z orbital perpendicular to the (111) plane. This highly oriented occupied state is probed by STM when the sample bias is negative. When the surface is probed with a positive sample bias, the unoccupied states of the surface are analyzed (data not shown). Hence bright spots in positive polarization are a signature of the Si atoms [88].

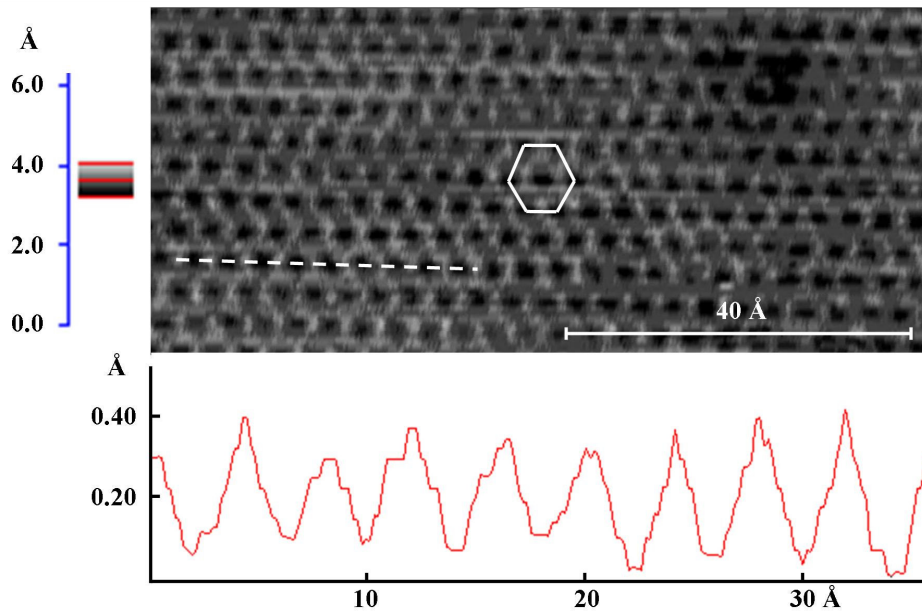


Figure V-8. As/Si(111) STM picture (drift-corrected): $I = 0.4$ nA and $V = -1.8$ V.

V.2.B. LEED characterization

In Figure V-9, LEED patterns are displayed for different incident beam energies: a) 51.8 eV, b) 64.3 eV and c) 102.0 eV. From these patterns, the lattice parameter can be calculated: $a_{\text{As/Si(111)}} = 0.379 \pm 0.004$ nm. Compared to the theoretical value of 0.384 nm for a pseudomorphic growth of arsenic on silicon, the relative error is 1.3%.

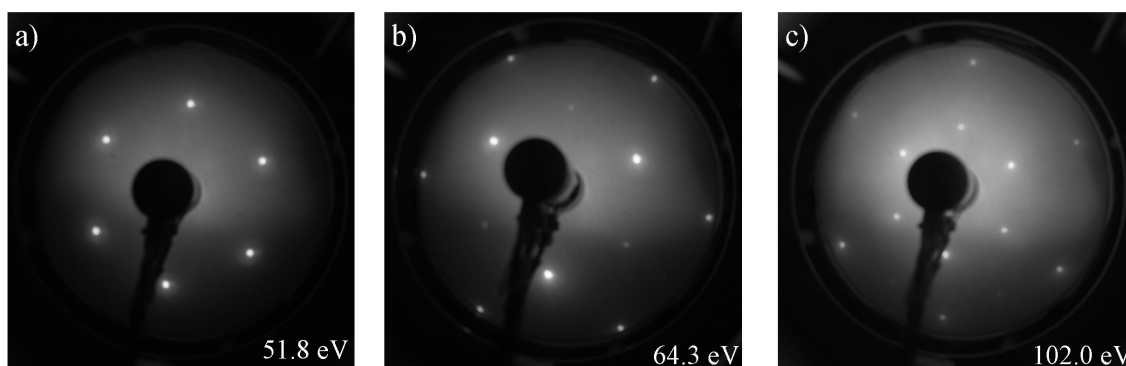


Figure V-9. LEED patterns of As/Si(111).

Depending on the energy of the primary beam, the intensities of the diffracted spots are different. This means that the intensity profile along a diffracting line of the reciprocal space is not constant; it depends on the properties of the nodes (according to the interference condition) which intersect the Ewald sphere. This modified spectrum of intensity can be explained by the change in the apparent crystallographic structure of the substrate due to the arsenic passivation.

In the (111) orientation, the arsenic atoms replace the top layer of Si. In LEED, the incident beam probes 2 layers of the substrate because of the penetration depth associated to electrons with an energy range between 30 and 150 eV. These electrons encounter a layer of arsenic atoms followed by a layer of silicon atoms. For the incident beam, it is equivalent to the first bi-layer of a zinc blende structure. Hence, the first conclusion is that the reciprocal space to be considered is the zinc blende one. The probed thickness is only two layers, thus the incident beam is diffracted by a quasi 2D surface. This is the second conclusion: the corresponding reciprocal space is not a set of rods but rather a set of elongated points, making lines with an inhomogeneous intensity profile.

In order to prove that the intersection between the Ewald sphere and the reciprocal lattice results in a LEED pattern with a “breathing” intensity for each diffraction spot, a FORTRAN program is implemented to simulate the diffracted intensity. As a starting point, it is necessary to know the structure factor at a position (hkl) of the reciprocal lattice. As stated in Chapter II, this factor S_{hkl} depends on the form factor of each atom creating the real space unit cell. These form factors f_j reflect the diffracting power of each atom and fluctuate with the nature of the probing beam. Indeed, X-rays interact with the electrons of the substrate whereas for incident

electrons, the associated wave interacts with the atomic internal electrostatic potential. In both cases, diffraction can occur because the electron distribution and the internal electric potential are both periodic in the crystal. For X-ray and electron incident beams, the mathematical model of the structure factor is the same, one term related to the diffracting power at a position \mathbf{r} in the real space (I) and a second term containing a phase factor (II). Conditions on the phase factor lead to destructive or constructive interference between the diffracted beams (see Chapter II):

$$S(\mathbf{G}) = \sum_{j=1}^n \underbrace{f_{j,s}(\mathbf{G})}_I \cdot \underbrace{e^{-i(\mathbf{G}, \mathbf{r}_j)}}_{II} \quad (5.1)$$

where n is the number of atoms in the unit cell, \mathbf{G} is a vector of the reciprocal space, \mathbf{r}_j is the position of the j^{th} atom in the unit cell (with one atom at position (0,0,0)) and s refers to X-rays (X) or electrons (e) for the incident beam. Let's define $f_{j,X}$ and $f_{j,e}$:

- X-rays interact with the electrons. Hence, the diffracting power of the atom j is obtained by integrating in the whole space the distribution of the electronic structure around the atom j ($n_{j,e}$). The weight of each point at a distance \mathbf{r} from the center of atom j depends on the diffraction direction (\mathbf{G}) and the distance itself:

$$f_{j,X}(\mathbf{G}) = \int_V n_{j,e}(\mathbf{r}) \cdot e^{-i(\mathbf{G}, \mathbf{r})} d\mathbf{r}; \quad (5.2)$$

- Electrons interact with the atomic potential $\phi(\mathbf{r})$ with the origin chosen at the center of the atom. Using the Poisson equation for a neutral and spherical isolated atom: $\nabla^2 \phi(\mathbf{r}) = -4\pi e [n_{j,p}(\mathbf{r}) - n_{j,n}(\mathbf{r})]$ with e the elementary charge, $n_{j,p}$ the positive charge distribution in the nucleus and $n_{j,n}$ the negative charge distribution in the electronic cloud [89, 90], the Mott-Bethe formula can be derived in terms of the form factor for X-rays:

$$f_{j,e}(\mathbf{G}) = \frac{2\pi m e^2}{h^2 \epsilon_0} \left[\frac{Z_j - f_{j,X}(\mathbf{G})}{|\mathbf{G}|^2} \right] \quad (5.3)$$

with Z_j the atomic number of the diffracting atom.

Writing 2θ the angle between the incident (\mathbf{k}_i) and diffracted (\mathbf{k}_f) wave vectors and according to the diffraction condition $\mathbf{G} = \mathbf{k}_f - \mathbf{k}_i$, the reciprocal vector \mathbf{G} can be expressed as a function of θ and λ (the wavelength associated to the X-rays or the electrons):

$$|\mathbf{G}| = \frac{4\pi \sin \theta}{\lambda} \quad (5.4)$$

For electrons, λ can be written as: $\lambda = \frac{h}{mv}$ where h , m and v are respectively the Planck's constant, the mass and the speed of an electron. This expression of λ and equation (5.4) leads to:

$$f_{j,e} \left(\frac{\sin \theta}{\lambda} \right) = \frac{e^2}{8\pi\epsilon_0 m v^2} \left[\frac{Z_j - f_{j,x} \left(\frac{\sin \theta}{\lambda} \right)}{\sin^2 \theta} \right] \quad (5.5)$$

The difference between the form factors for X-rays and electrons results in dramatic consequences:

- The speed of the electrons (v) is much lower than the light speed (c) of X-rays; hence the amplitude of the form factor is higher in the case of electron diffraction. In other words, the diffracted intensity is more intense in the case where a primary beam of electrons is used;
- For electron diffraction, the interaction between the incident and diffracted beam is stronger because the diffracted beams emerge all from the top two or three layers of the sample. Among the two models developed hereafter for the discussion of the diffracted intensity (I_{diff}), the dynamical model is more suitable for the interaction of electrons with the surface whereas the kinematical model can only be used as a first approximation. However, it is easier to implement the kinematical model in a theoretical simulation;
- For electron diffraction, the diffracting power is highly dependent on the diffraction angle;
- Assuming a spherical symmetry for the negative charge distribution and if $\theta = 0$ or π , the form factors are [91, 92]:

$$\begin{aligned} f_{j,x}(0) &= Z_j \\ f_{j,e}(0) &= \frac{4\pi m e^2}{3h^2} Z_j \langle r_j \rangle^2 \end{aligned} \quad (5.6)$$

where Z_j is the atomic number of the atom j and $\langle r_j \rangle$ is the mean radius of atom j . For electrons, the form factor is not only depending on Z_j then this property can be used to sort out atoms hardly distinguishable by X-ray diffraction.

Quantum mechanics calculations can provide the electronic density as a function of the distance from the center of the atom and from this density, the form factor can be plotted as a

function of $\frac{\sin \theta}{\lambda}$. Figure V-10 shows the form factor for Si (dashed line) and As (solid line) as a function of $\frac{\sin \theta}{\lambda}$ for incident X-rays (Figure V-10a) and electrons (Figure V-10b), using the values from Wilson *et al.* [93].

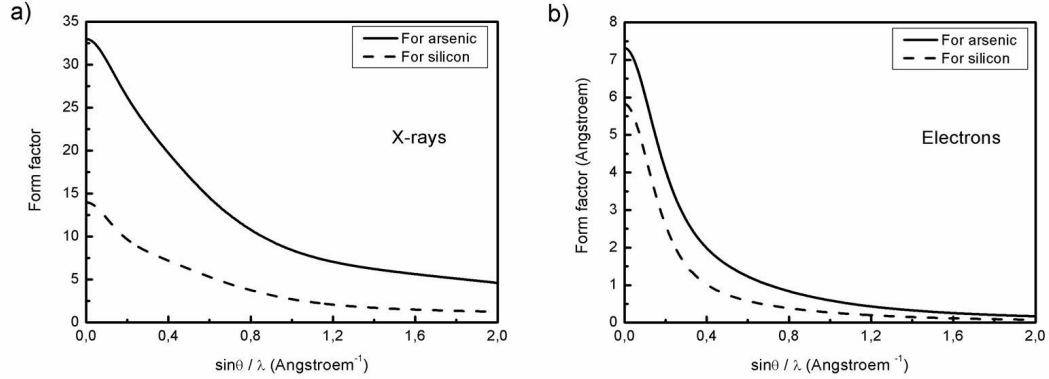


Figure V-10. Form factors for an incident beam of a) X-rays and b) electrons as a function of $\sin \theta / \lambda$.

Concerning the total diffracted intensity (I_{diff}), two models have been developed:

- The kinematical model which neglects the interaction between the incident and the diffracted beams. This approximation is valid when the diffracted intensity is weak compared to the incident intensity. This is merely true for a set of parallel X-ray beams hitting the surface or for a substrate consisting of small crystallites. In this model, the diffracted intensity is proportional to $S_{hkl} \cdot S_{hkl}^*$;
- The dynamical model, developed by Darwin [94-96], considers the interaction between the incident and the diffracted beams. The phase between two consecutive bi-planes is π , leading to a decrease in the total diffracted intensity. This is particularly true for a perfect crystal or an incident beam composed of electrons because these particles produce numerous diffracted beams compared to X-rays. This is due to the higher diffraction cross section of electrons. In the dynamical model, the intensity is proportional to $S_{hkl} \cdot S_{hkl}^* \cdot \frac{\tanh(\pi t / \Lambda)}{\pi t / \Lambda}$ where t is the thickness of the perfect crystal

(depending on the dislocation density) and Λ is the Pendellösung distance (or the extinction distance) [97, 98]:

$$\Lambda = \frac{V}{r_e P |S_{hkl}| \lambda} \quad (5.7)$$

with λ the wavelength of the electrons, V the volume of the elementary cell, r_e the classical radius of the electron, F the structure factor and p the polarization factor. The factor multiplying $S_{hkl} \cdot S_{hkl}^*$ is a value between 0 and 1. If $t \gg \lambda$ the dynamical theory is applicable, otherwise the kinematical theory is dominant;

- Most of the time, the real crystal is not perfect but more ordered than a set of crystallites. Hence, the diffracted intensity is in between the kinematical and the dynamical models, and proportional to $\left(\sqrt{S_{hkl} \cdot S_{hkl}^*}\right)^\alpha$ with $1 \leq \alpha \leq 2$;
- In both cases, the structure factor appearing in the diffracted intensity calculation is a temperature dependent variable:

$$S_{hkl}^T = S_{hkl}^{0K} \cdot e^{-2M} \quad (5.8)$$

where M is the Debye – Waller factor: $M = \frac{8\pi^2 \langle u^2 \rangle \cdot \sin^2 \theta}{\lambda^2}$ with $\langle u^2 \rangle$ the mean square value of the atomic vibration amplitude from the equilibrium position.

V.2.C. LEED simulation

The detailed FORTRAN program written in order to simulate the LEED intensities is presented in Annex 4. Hereafter are the main considerations and the result of the simulation for an incident beam energy of 64.3 eV.

LEED pattern of As/Si can be seen as the diffraction on the top layers of a zinc blende crystallographic structure. Hence the first part of the program consists of modeling the 3D reciprocal lattice of the zinc blende structure (Figure V-11a). The structure factor associated to the nodes in the reciprocal space depends on the (hkl) position and the form factors. In the figure, blue, red and yellow nodes represent a high, medium and low diffracting power respectively. The form factor associated to each node depends on the diffraction angle and the wavelength of the electrons (see (5.5)). In the program, the angle between the incident and diffracted wave vectors is calculated and knowing the incident beam energy, one can deduce the form factor for As and Si from Figure V-10.

Considering that the real space is (111) oriented and that the incident wave vector intersects a blue node, two views of the reciprocal space are presented in Figure V-11b and c. In the [111] direction of the reciprocal space (Figure c), three sets of lines can be defined: denoting Z the

distance between two nodes along the [111] direction, the sets are shifted by a value $Z/3$ to each other. These sets are represented by dots, crosses and triangles in Figure V-12.

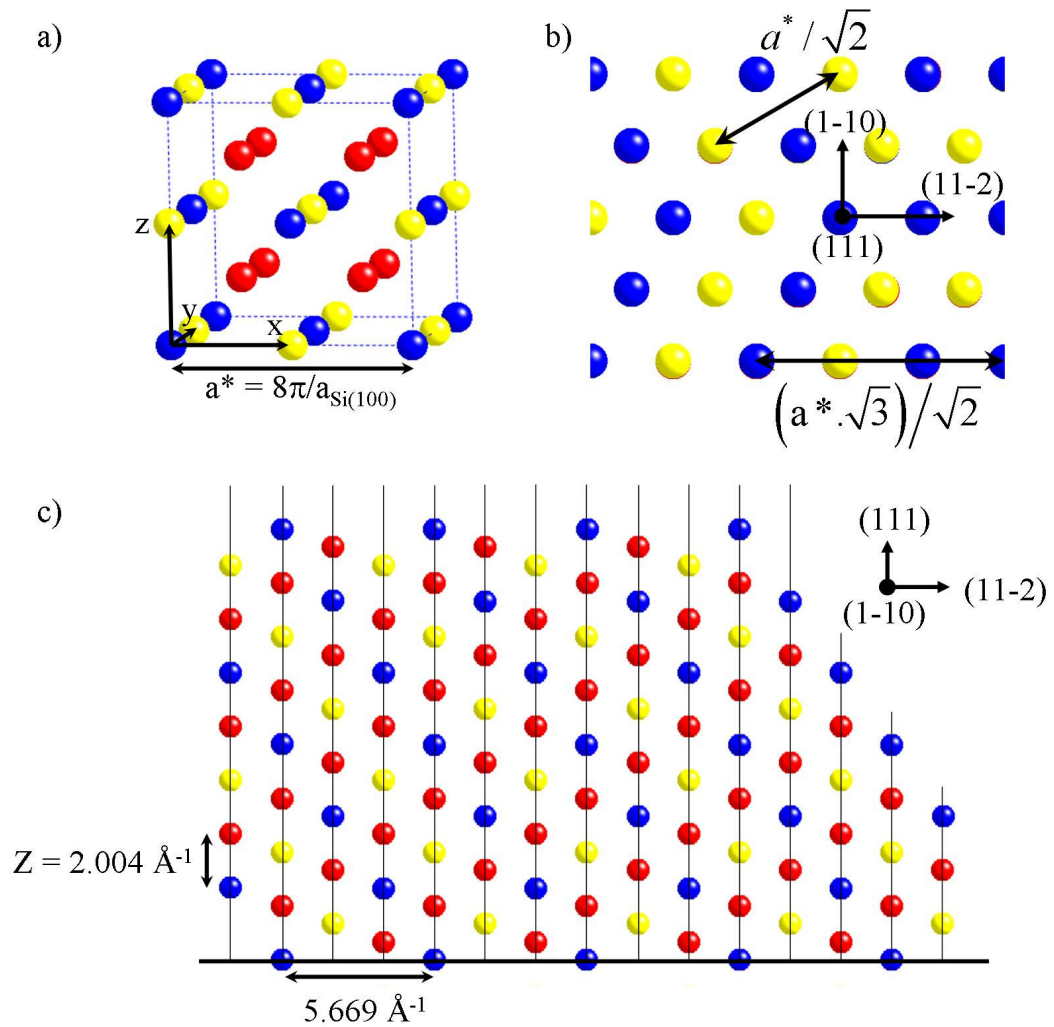


Figure V-11. a) Reciprocal lattice of As/Si zinc blende structure; b) Top view in the (111) direction and c) nodes along the [111] direction.

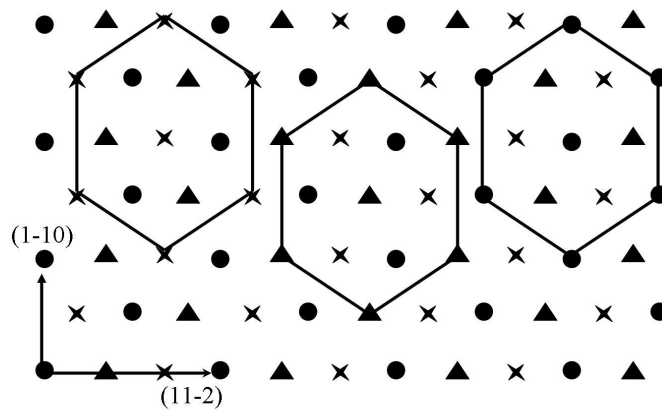


Figure V-12. (111) reciprocal planes. Symbols represent nodes of the reciprocal lattice at different heights.

In order to take into account the fact that the diffracting crystal consists of a quasi 2D structure instead of a 3D structure, the nodes of the reciprocal space are broadened by a Gaussian centered on the node. Hence, for the diffraction, the intensity profile is not a set of Dirac peaks centered at each node along the [111] direction but a continuous intensity profile as presented in Figure V-13 for the three different kind of rods. The relative intensity of the peaks depends on the diffracted intensity by each point of the reciprocal space: the kinematical model is preferred to the dynamical model because it is easier to implement in the program and the kinematical model is a good first approximation when the wavelength associated to the electrons is close to 1 Å [97]. Hence, the diffracted intensity is proportional to $S_{hkl} \cdot S_{hkl}^*$ and the structure factor itself is a function of the form factor whose value depends on the diffraction angle (θ) and the wavelength associated to the electrons (λ). So, in the program, the intersection between the Ewald sphere and the points of the reciprocal space is first calculated. The possible diffraction angles are then calculated and from these values, the form factors are inferred from Figure V-10 for each angle. Using these parameters, the diffracted intensity is normalized and the program is run again to obtain the diffracted intensities. For example, for a primary beam energy of 64.3 eV (i.e. $\lambda = 0.153$ nm), two diffraction angles are calculated: 70° and 46°. For an angle of 70°, the form factors of As and Si are respectively 1.21 and 0.57 and for an angle of 46°, these values become 3.87 and 2.41. These form factors for each angle of diffraction and the calculation of the diffracted intensities are given in Table V-3 for each kind of node of the reciprocal space (related colors). The simulated diffraction pattern using these settings is given in Figure V-14b. The relative intensity of the diffraction spots is in agreement with the LEED pattern picture of Figure V-9b. The same principle is followed to simulate LEED patterns with an incident energy of 51.8 and 102.0 eV (Figure V-14a and c), to be compared to Figure V-9a and c.

The last point consists of verifying that the relative intensities of the diffraction spots in a pattern are also modeled by the program for a wider range of energy. For the inner spots of Figure V-9a to c, the relative intensities between the mean value (calculated on 30 pixels) of the three brighter and the three darker spots are measured with ImageJ (free software available online) and presented in the second column of Table V-4. The errors are obtained by calculating the standard deviations. The ratios calculated from the intensities given by the FORTRAN program are displayed in the third column and relative errors between the experimental and modeled ratios are presented in the last column. It is obvious from these

calculations that the simple model developed in this section is a good approximation to explain the diffraction patterns obtained by LEED.

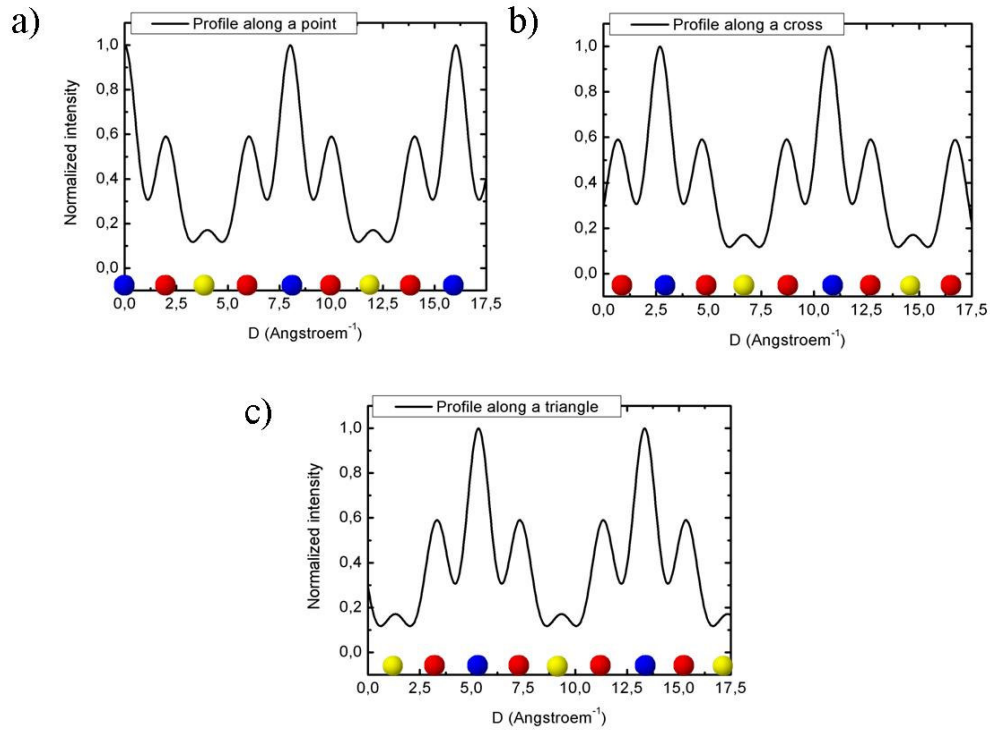


Figure V-13. Gaussian profiles along the [111] direction for a) points; b) crosses and c) triangles of Figure V-12. D represents the distance along the [111] direction from a plane containing the end of the incident wave vector.

$\theta = 70^\circ$ and $\lambda = 0.153 \text{ nm} \Rightarrow f_{As} = 1.21$ and $f_{Si} = 0.57$			
$h + k + l$	S_{hkl} (see Chapter II)	Weighted intensity (a.u.)	Normalized intensity
$4n$	$f_{Si} + f_{As}$	$(f_{Si} + f_{As})^2 = 3.17$	1
$4n + 1$	$f_{Si} - i \cdot f_{As}$	$(f_{Si})^2 + (f_{As})^2 = 1.79$	0.56
$4n + 3$	$f_{Si} + i \cdot f_{As}$	$(f_{Si})^2 + (f_{As})^2 = 1.79$	0.56
$4n + 2$	$f_{Si} - f_{As}$	$(f_{Si} - f_{As})^2 = 0.41$	0.13
$\theta = 46^\circ$ and $\lambda = 0.153 \text{ nm} \Rightarrow f_{As} = 1.65$ and $f_{Si} = 0.83$			
$h + k + l$	S_{hkl} (see Chapter II)	Weighted intensity (a.u.)	Normalized intensity
$4n$	$f_{Si} + f_{As}$	$(f_{Si} + f_{As})^2 = 6.15$	1
$4n + 1$	$f_{Si} - i \cdot f_{As}$	$(f_{Si})^2 + (f_{As})^2 = 3.41$	0.55
$4n + 3$	$f_{Si} + i \cdot f_{As}$	$(f_{Si})^2 + (f_{As})^2 = 3.41$	0.55
$4n + 2$	$f_{Si} - f_{As}$	$(f_{Si} - f_{As})^2 = 0.67$	0.11

Table V-3. Normalized diffracted intensity for $E = 64.3 \text{ eV}$.

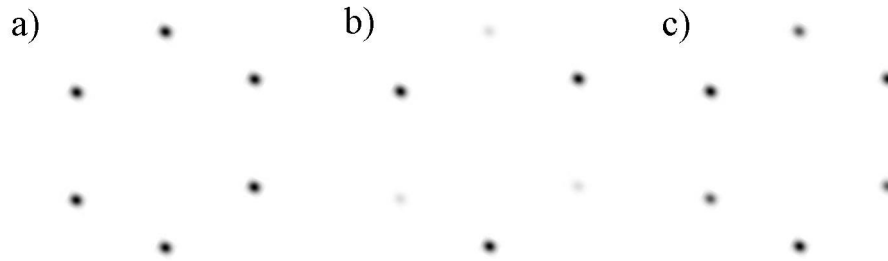


Figure V-14. Simulated LEED patterns for a) $E = 51.8$ eV; b) 64.3 eV and c) 102.0 eV.

Energy	Measured intensity ratio (ImageJ)	Calculated intensity ratio (FORTRAN)	Relative error
51.8 eV	1.12 ± 0.07	1.0	11 %
64.3 eV	6.2 ± 0.60	6.9	11 %
102.0 eV	1.32 ± 0.13	1.49	13 %

Table V-4. Ratios between the intensities of the brighter and darker inner spots of As/Si LEED patterns.

V.3. Growth of thick CdTe(211)B/ZnTe(211)B/As/Si(211)

The first aim of this work is to demonstrate that selective growth can be achieved on an optically lithographed CdTe layer grown on Si. Prior to selective growth and optical lithography, the first step consists of growing a high quality CdTe layer on Si. As explained in the historical part of this thesis, high quality CdTe with a B polarity can be grown on a Si(211) substrate if the Si surface is passivated with arsenic followed by the growth of a ZnTe buffer layer.

It was demonstrated that the RCA cleaning process can be used to produce a clean inert SiO₂ layer and that this oxide can be removed by annealing at 1050°C in UHV. The As passivation leading to a 1x1 reconstruction of the silicon surface was also achieved. These results and the details of the experimental procedures obtained on Si(111) can in principle be transposed to the case of Si(211) surface which consists of steps of (111) and (100) terraces.

The thick CdTe layer is grown at the University of Illinois at Chicago, in the OPUS 45 chamber. Si(211) double side polished wafers from Viginia Semiconductor with a diameter of 3 inches are used as substrates. The wafers properties are the following:

- Orientation: $(211) \pm 0.5^\circ$;
- Doping: p-type (boron doped);
- Resistivity: 30 – 70 Ωcm ;

- Crystal growth method: Czochralski;
- Thickness: $381 \mu\text{m} \pm 25 \mu\text{m}$.

The Si(211) substrate is outgassed for one night at 500°C in a preparation chamber before being transferred to the MBE chamber. Both chambers have a base pressure of 1.10^{-10} mbar. The MBE chamber is cooled with liquid nitrogen and the evaporation cells are connected to a closed water-cooling system.

The growth scheme is presented in Figure V-15 and implies four steps:

- Cooling under As_4 flux after oxide desorption at high temperature. The flux is interrupted when the thermocouple reads 400°C (T^*). After this first step, the RHEED pattern consists of sharp lines with a high contrast between the lines and the background, indicating a highly crystalline surface (data not shown);

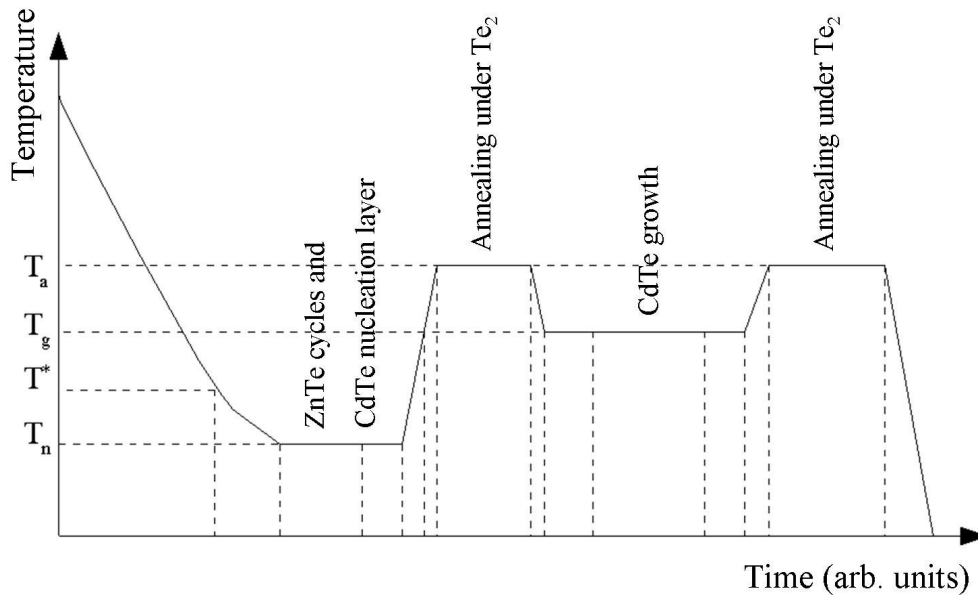


Figure V-15. MBE growth scheme for CdTe film.

- The second step is the growth of the ZnTe buffer layer by evaporation of one monolayer of tellurium followed by migration enhanced epitaxy (MEE) at a temperature $T_n = 340^\circ\text{C}$. A MEE cycle consists of the exposure of the sample to a Zn flux for 10 seconds, followed by no flux for 5 seconds then a Te_2 exposure for 10 seconds and finally no exposure to any flux for 5 seconds. The temperature of the cells is set so that a RHEED change is observed in 2 seconds when the sample is rotating at a frequency of 0.25 Hz. The buffer layer process is performed as follow:

- Exposure for 30 seconds to Te_2 to saturate the surface (RHEED change observed) followed by no flux exposure for 30 seconds;
- 40 MEE cycles of ZnTe growth.

At the end of this process, the RHEED pattern consists of wide rods (Figure V-16a). The poor quality is due to the low thickness of the ZnTe grown layer (about 10 nm), but the orientation of the pattern is a signature of the desired (211)B orientation of the layer [99]. The growth conditions for the cells temperature and the associated flux read on the gauge are 170°C and $2.0 \cdot 10^{-8}$ mbar for Zn and 240°C and $1.0 \cdot 10^{-7}$ mbar for Te_2 . Although the flux readings are different, the rate of the RHEED change is the same. The flux difference is due to the geometry of the MBE system and to the sensitivity of the gauge to the different gases;

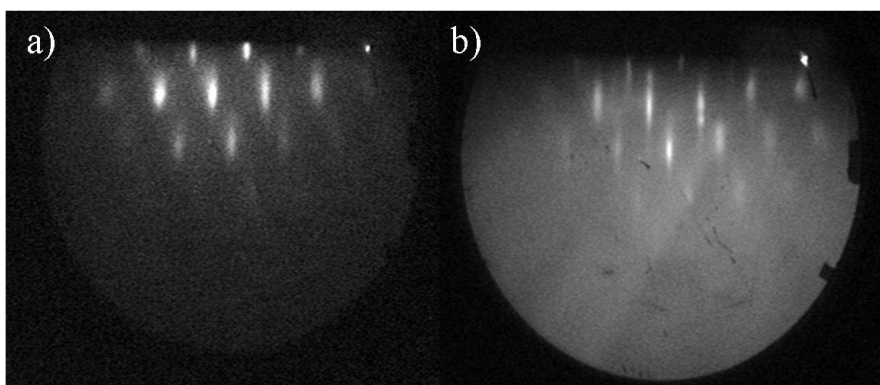


Figure V-16. a) ZnTe(211)B/As/Si(211) and b) 5 μm thick CdTe(211)B/ZnTe(211)B/As/Si(211) RHEED patterns in the [01-1] direction.

- Maintaining the nucleation temperature (T_n), a thin CdTe layer is grown for 2 minutes to ensure complete coverage of the surface (seen by RHEED transition). This nucleation at 340°C is followed by annealing of the substrate under Te_2 for 10 minutes with the substrate at 480°C (T_a). This annealing promotes a reconstruction of the layer to obtain a flat surface suitable for subsequent CdTe growth;
- The last step is the growth of a thick CdTe layer (about 5 μm) with the substrate at 440°C (T_g). The CdTe cell is heated to 545°C which is a temperature required to obtain a growth rate of about 1 μm per hour. At the end of the growth, the sample is set to T_a and annealed for 10 more minutes under Te_2 before being cooled down to room temperature. The RHEED pattern at the end of the growth process is presented in

Figure V-16b. The orientation and the width of the lines are a proof that the layer follows the (211)B orientation and that the quality of the layer is good.

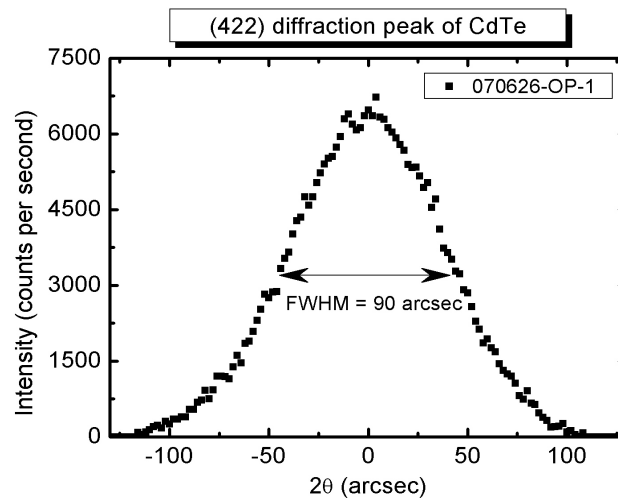


Figure V-17. FWHM of CdTe(422) diffraction peak by DCRC-XRD.

XRD experiment confirms the monocristallinity of the surface: only the (422) peak is detected, in agreement with the systematic extinction theory for zinc blende structure leading to the vanishing of the (211) diffraction peak. DCRC-XRD characterization points out the quality of the grown layer by measuring the full width at half maximum of the diffraction peak. Figure V-17 shows the (422) diffraction peak obtained by DCRC-XRD on a 12 μm thick CdTe(211)B/ZnTe(211)B/As/Si(211) layer grown according to the same procedure described above. The given thickness is the mean value of several FTIR (Fourier Transform Infra Red Spectroscopy) measurements. The FWHM is 90 arcsec and this value has been routinely observed with repeated growth experiments.

V.4. Growth curve and sticking coefficient by MBE

The heating system of the LPEM MBE system has to be calibrated and the sticking coefficient of CdTe needs to be determined for different substrate temperatures. These studies are necessary to analyze the selective growth conditions and to explain the mechanism involved in the selectivity.

V.4.A. Temperature calibration of the MBE

A Si(211) sample is mounted on a molybdenum PEEM sample holder (back side of the sample at 1 mm from the heater and the front side is windowed to see the surface). A K-type thermocouple is glued with In on the surface of the silicon piece. The sample is heated by

radiation for 15 minutes before measuring the thermocouple voltage. This delay ensures that the sample temperature is stabilized. The experimental points corresponding to two sets of measurements are represented by the squares and triangles in Figure V-18.

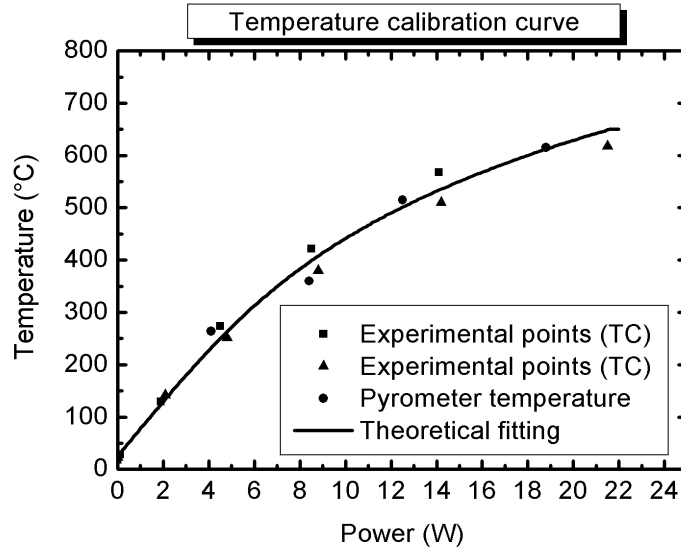


Figure V-18. Temperature calibration for radiative heating in the LPEM MBE system.

Another Si(211) sample is loaded in the MBE chamber without any thermocouple. A pyrometer is focused on the window of the sample holder to measure the surface temperature. The emissivity of the pyrometer is adjusted so that the read temperature matches the temperature measured previously with the thermocouple under the same heating power conditions. The pyrometer measurements are represented by the circles in Figure V-18.

The experimental points are then fitted by a theoretical curve which expresses the relationship between the heating power in watts (W) with respect to the temperature in Celsius degrees (°C):

$$P(T) = -0.49 + 0.019 T + 5.40 \cdot 10^{-11} T^4 \quad (5.9)$$

This equation is derived from the conversion of the heating power into radiation (Stefan's law) and conduction ($\propto T$) losses. The fit of the inverse function ($T(P)$) is the solid line in Figure V-18.

V.4.B. Growth rate of CdTe on ZnTe(211)B/As/Si(211)

It is known from literature that a growth rate around 1.0 μm per hour leads to CdTe layers showing the highest crystalline quality.

This section is dedicated to the determination of CdTe growth rate for a given flux of CdTe and for different substrate temperatures. The substrate used in this case consists of a 10 nm thick ZnTe(211)B layer grown by MBE on As/Si(211) and cleaned according to the following wet etching process:

- Rinsing in methanol;
- Dipped for 1 second in HBr:H₂O:H₂O₂ in concentration 5:90:1;
- Rinsing in methanol and blowing dry with nitrogen.

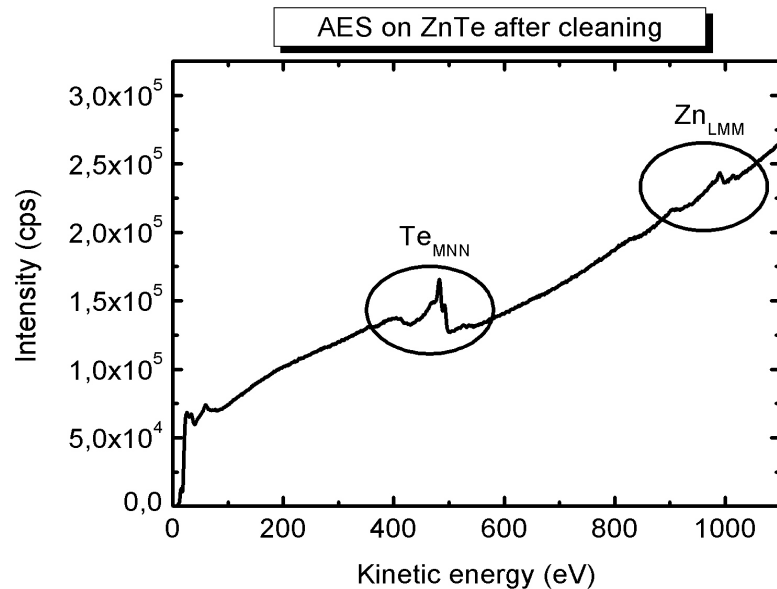


Figure V-19. AES on ZnTe after ex-situ and in-situ cleaning.

After this chemical cleaning, the Te-rich ZnTe substrate is mounted on a molybdenum sample holder (same geometry as the sample holder used for the temperature calibration) and loaded in the UHV system. The sample is sputtered with Ar⁺ ions with a kinetic energy of 1 keV for 2 minutes. An annealing at 350°C for 15 minutes followed the sputtering to desorb the argon atoms implanted in the matrix. Auger electron spectroscopy (Figure V-19) confirms that this treatment promotes clean ZnTe surfaces suitable for MBE growth.

In the MBE chamber, the sample is exposed to a CdTe flux of $1.0 \cdot 10^{-7}$ mbar for 90 minutes. 8 samples were grown at different temperatures. The samples are then removed from UHV and completely etched on the half of the sample. From the step created, the CdTe layer thickness can be estimated by using profilometry. For simplicity, the measured heights are converted into growth rate expressed in ML/s (Figure V-20).

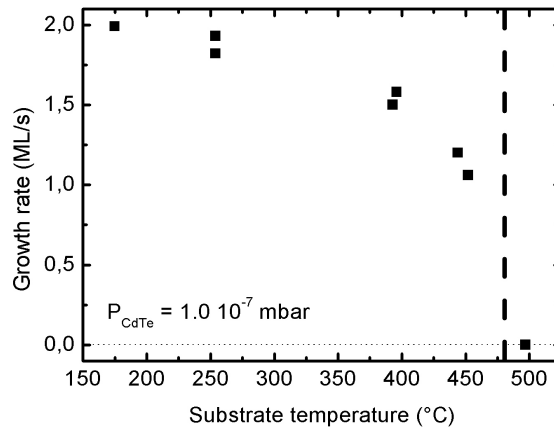


Figure V-20. a) Growth of CdTe on ZnTe for $P_{\text{CdTe}} = 1.0 \cdot 10^{-7}$ mbar.

The last step needed to know all the conditions required to achieve selective growth is the determination of the highest nucleation temperature of CdTe on Si. For this experiment, a modified RCA cleaned Si(211) is loaded in the UHV system and outgassed at 500°C overnight and the oxide is flashed out at 1050°C in the MBE chamber. The sample is cooled to 540°C and exposed to a CdTe flux of $1.0 \cdot 10^{-7}$ mbar for 2 minutes. If no change is observed in the RHEED pattern, the sample temperature is decreased by 20°C and the sample is exposed to the same flux for the same time. For the present flux of CdTe, the highest nucleation temperature for CdTe on Si(211) is between 455 and 480°C (dashed line in Figure V-20). It is obvious from Figure V-20 that at this upper limit temperature, the sticking coefficient of CdTe on CdTe is not equal to zero. In conclusion, for a given flux of CdTe, a sample temperature window can be found where selective growth of CdTe can be observed. If the CdTe flux increases, one can expect the curve in Figure V-20 to move to the north-east and the dashed line to move to the east.

V.5. Optical lithography

To demonstrate the feasibility of selective growth by MBE, the first study consists of CdTe that will be grown on patterned substrates consisting of CdTe islands on silicon. This section describes the fabrication of such samples by optical lithography.

V.5.A. Optical lithography: fundamentals

A quick and widespread method for the creation of structures in the micron size range is optical lithography. The basic idea is firstly to spin coat a photoresist on the surface. Second, a mask is positioned close to the surface using a mask aligner and the sample is illuminated

with UV light (Figure V-21a) which burns the exposed photoresist. The third step consists of dissolving the burnt (positive lithography) or not burnt (negative lithography) photoresist with an adequate solvent (Figure V-21b for negative lithography). The next step is the key point of the lithography process: the etching of the regions that are no longer protected by the photoresist. Two etching processes are used in the experiments carried out in this thesis:

- Dry reactive ion etching (DRIE): the sample is exposed to etching ions. Both chemical and physical etchings contribute together. In optimum conditions (concerning the gas mixture, concentrations and energy of the ions), anisotropic etching is achieved, leading to very sharp edges for the islands. This etching has to be carried out when the ratio patterned structure diameter/thickness is small. Because of the cost and the time needed to optimize the experimental conditions, this technique is mostly useful to etch nanometer scale structures (Figure V-21c);

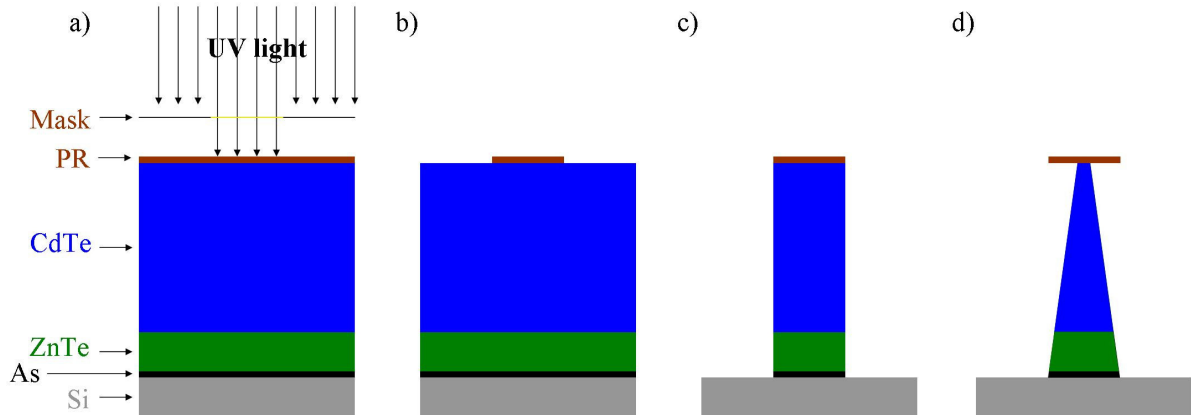


Figure V-21. Optical lithography process: a) UV light illumination; b) negative lithography dissolution; c) patterning by dry etching; d) patterning by wet etching.

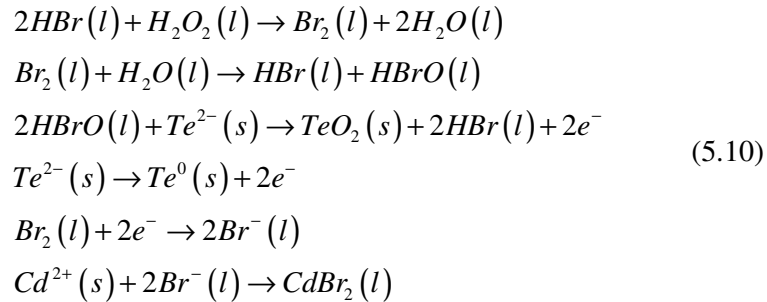
- Wet etching: the sample is immersed in a chemical solution dissolving the layer without altering the remaining photoresist. The inconvenient of this technique is that it is mostly isotropic. Hence the chemical agent etches also the side of the island, leading to final structures with a pyramidal shape (Figure V-21d). However, this technique is very quick and cheap compared to dry etching. It is particularly useful when the ratio patterned structure diameter/thickness is high.

The remaining photoresist can then be dissolved in acetone to obtain the final structure.

V.5.B. Optical lithography of a 2 μm-thick CdTe(211)B layer

A 2 μm thick CdTe(211)B/ZnTe(211)B/As/Si(211) layer is grown by MBE according to the growth procedure described earlier (see section V.3.). The film is exposed to atmosphere and an organic negative photoresist (SPR 1818) is spin coated for 40 seconds at 3000 rpm onto the sample before being baked at 75°C for 40 minutes. Before the spin coating, the sample is chemically cleaned with acetone and methanol for 60 seconds before being rinsed in DI water and blown dry with nitrogen. A mask is placed close to the CdTe layer in a Karl Suss mask aligner and exposed to UV light for 11 seconds. The mask consists of holes transparent to the UV light with a diameter of 80, 100, 160, 210, 260 and 310 μm. In the exposed regions, the binding of the photoresist is reinforced; when the sample is dipped in the developing solvent (CD-351 solution diluted with DI water in a proportion 1:3) for 12 seconds, the unexposed regions of the photoresist are dissolved.

Wet etching is used to remove the CdTe uncovered by the photoresist remaining after the development in the solvent. Bromine based solution is a well known chemical etchant for CdTe [100-102]. In this case, a mixture of HBr, H₂O₂ and DI water is used in the ratio 10:1:50. The hydrobromic acid reacts with hydrogen peroxide to produce bromine (Br₂); an oxido-reduction reaction between Br₂ and Te²⁻ leads to the formation of metallic tellurium and the Br⁻ ions react with Cd²⁺ to form CdBr₂. Moreover, bromine also reacts with H₂O, producing HBrO, a compound reacting also with Te²⁻ to produce an excess of tellurium dioxide (TeO₂) on the surface:



The metallic tellurium remains on the surface because of the poor probability of TeBr₄ formation [103]. The tellurium atoms aggregate to form a cluster and the stress appearing at the CdTe – Te cluster interface is the driving force favoring the removal of Te in the form of aggregates.

The results of the wet etching of CdTe(211)B with HBr:H₂O₂:H₂O are tellurium – rich columns covered by a cap of photoresist. This organic cap can easily be removed by dipping in acetone. The patterned substrate is characterized by scanning electron microscopy (SEM) (Figure V-22a) and profilometry (Figure V-22b) to check the spatial distribution and the height of the pillars. This height is the reference for a further selective growth process and is measured on several pillars with a diameter of 80 μm . The mean measured height is 0.90 μm \pm 0.02 μm .

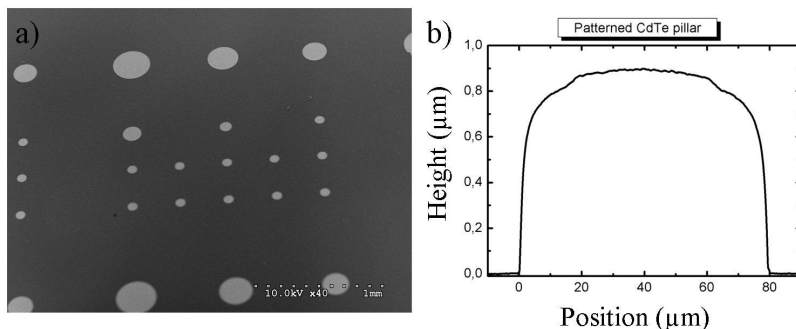


Figure V-22. a) SEM picture of CdTe islands on Si(211); b) profilometry line profile of a CdTe pillar.

All the following in-situ experiments are carried out with the LPEM UHV equipment composed of 4 chambers and a load lock. The first chamber is a preparation chamber connected to the load lock. This chamber is equipped with a carousel containing up to 8 samples and a heater (dedicated to radiative and direct heating). From this chamber, the sample can be transferred into the 3 other chambers. The second chamber is a customized MBE chamber from RIBER equipped with radiative and direct heating systems, RHEED equipment and evaporation cells containing Te₂, As₄ and CdTe. The third part is a room temperature STM chamber and the last chamber is the analysis chamber. This latter chamber is equipped with facilities for LEED, AES and PEEM. A heater can be used for radiative or direct heating of the substrate (Figure V-23).

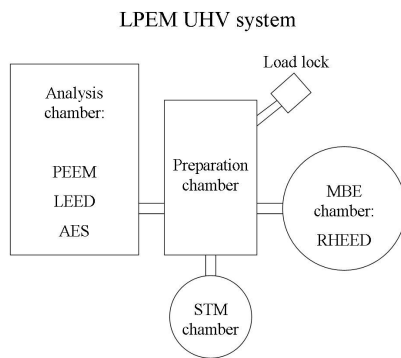


Figure V-23. UHV system at LPEM.

V.5.C. Desorption of the excess of Te

The excess of Te due to the chemical wet etching has to be desorbed under UHV environment before checking the feasibility of selective growth. For this study, a patterned sample is etched for 5 seconds in a freshly made bromine/methanol solution (0.1 %) and quickly loaded in the UHV system to perform PEEM experiment. The UV source of the PEEM is a Hg lamp with a photon energy of 4.9 eV. In Table V-5, the workfunction of Te, Si, As (from [104]), CdTe [105] and SiO₂ [106, 107] are presented.

Element	Workfunction (eV)
Te	4.04
Si	4.52
As	5.11
CdTe	5.9
SiO ₂	4.52

Table V-5. Workfunction of Te, Si, As, CdTe and SiO₂.

Thanks to the photon energy of the Hg lamp, the metallic Te on the Te-rich CdTe pillar (region I in Figure V-24a) can be observed by PEEM. In this figure, the region II (corresponding to a thin SiO₂ layer covering the Si) appears dark because of the voltage applied to the multichannel plate (MCP): the signal arising from Te is so intense that the MCP is set to a low voltage to avoid damages. After annealing at 350°C for 1 minute, the PEEM picture is completely different (Figure V-24b). The region II related to SiO₂ is bright because the associated workfunction is lower than the energy of the exciting UV light and the MCP voltage is set to a higher value. On the contrary, the region III is dark and corresponds to a CdTe island after desorption from the excess of metallic tellurium. The workfunction of CdTe is higher than the energy of the UV light so that no electron is emitted from this part of the surface.

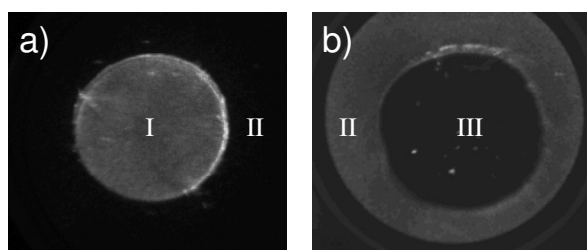


Figure V-24. PEEM picture of CdTe pillar with a diameter of 80 μm . a) Before excess Te desorption; b) after Te desorption at 350°C.

V.6. Selective growth on CdTe seeds patterned on SiO₂

For this experiment, the growth is realized in the LPEM MBE system.

A patterned CdTe sample is etched in a bromine-methanol solution (0.1%) for 5 seconds, blown dry with nitrogen and loaded in the UHV system. The excess of tellurium is desorbed by heating the substrate at 350°C for 1 minute in the analysis chamber.

Two experiments at different substrate temperatures were realized. According to section V.4.B., the highest nucleation temperature of CdTe on Si(211) occurs with a substrate temperature between 455 and 480°C when exposed to a CdTe flux of $1.0 \cdot 10^{-7}$ mbar. Hence, for the first growth on a CdTe patterned sample, the substrate temperature is set to 480°C and the temperature is 490°C for a second experiment. In both cases, the sample was exposed to a CdTe flux for 2 hours, but the CdTe flux was different.

PEEM characterization is performed after Te desorption and after CdTe growth to observe the possible selective process. The height of the islands is measured ex-situ with a profilometer. For these experiments, the profilometry and PEEM analysis presented in Figure V-22b and Figure V-24b are the reference measurements.

V.6.A. Growth at 480°C

With a substrate temperature of 480°C and after being exposed to a CdTe of $3.0 \cdot 10^{-7}$ mbar for 2 hours, the diameter of the smallest pillars of the pattern is drastically increased (Figure V-25a). This measure is in agreement with the profilometry characterization: the height after the growth is about 10.81 μm (Figure V-25b), to be compared with the initial reference height of 0.90 μm .

Moreover, additional structures are observed between the islands (Figure c). These structures are very rough and their shape is random (Figure d). Hence the conclusion is that the growth is not selective with a substrate temperature of 480°C.

It is easy to explain why additional features are observed by PEEM. Indeed, the substrate temperature is set to 480°C, which is the upper temperature limit to observe nucleation of CdTe on silicon when the substrate is exposed to a measured flux of $1.0 \cdot 10^{-7}$ mbar. In this

case, the flux is slightly higher ($3.0 \cdot 10^{-7}$ mbar) in order to ensure a sufficient growth rate. The selective growth could be expected because this upper limit was for nucleation on clean Si. One can expect the nucleation on SiO_2 to be more difficult because the surface is less reactive. However, it is obvious from the experiment that at the same time the highest nucleation temperature on silicon is increased. Hence even if it is reasonable to assume that the growth rate on silicon is very low compared to the growth rate on CdTe because of the difference between the sticking coefficients, small structures of CdTe may appear on the exposed silicon surface between the islands after prolonged exposure to the CdTe flux. Once these additional structures appear, they act as seeds for the subsequent molecules of CdTe arriving on the surface, with a higher sticking coefficient and hence a higher growth rate.

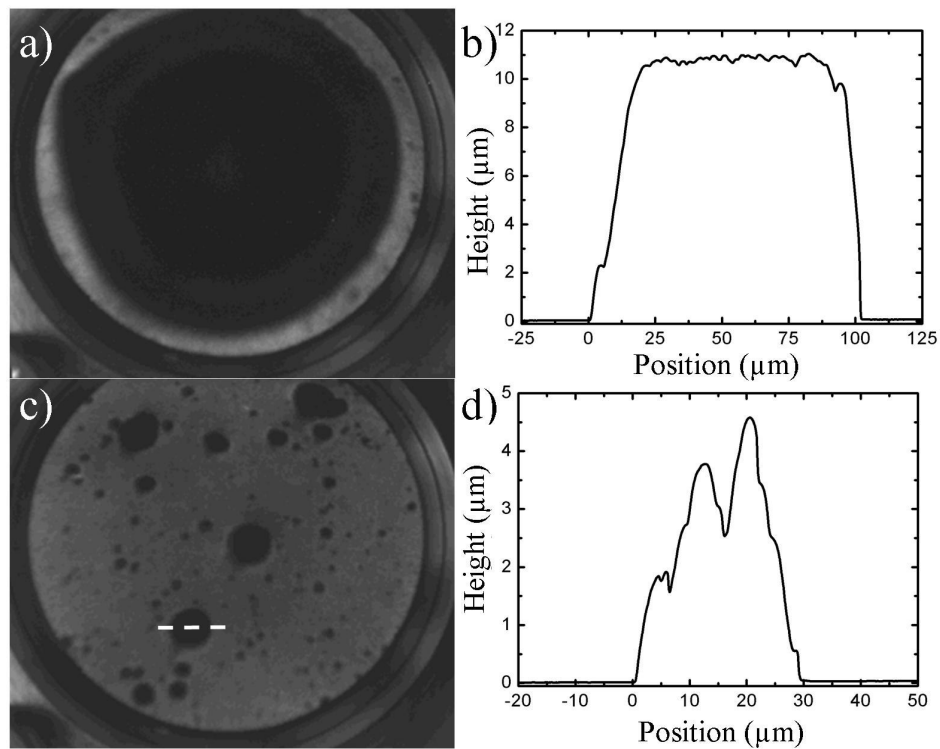


Figure V-25. Growth at 480°C: a) PEEM image of CdTe pillar; b) height of the pillar by profilometry; c) PEEM image between the islands; d) height of the dashed line in figure c) by profilometry.

The results of the growth rate and the standard deviation of the height (indicator of the growth quality) for the initial islands and the additional features appearing on the surface are respectively presented in columns 2 and 3 of Table V-6. The first column contains the reference values arising from the measurement of a patterned substrate unexposed to CdTe.

The growth rate on the CdTe pre-existing pillars is higher (1.4 nm/s) compared to the growth rate on the additional structures (0.35 nm/s) because the growth rate is a mean value and that the real time for growth on CdTe pillars or on seeds of CdTe freshly adsorbed is different.

	Reference patterned sample	Growth at 480°C ($p_{\text{CdTe}} = 3.0 \cdot 10^{-7}$ mbar)		Growth at 490°C ($p_{\text{CdTe}} = 1.0 \cdot 10^{-7}$ mbar)
		Island	Additional structure	
Height (μm)	0.90	10.81	2.52	1.53
Standard deviation (μm)	0.02	0.13	1.22	0.02
Growth rate (nm/s)	-	1.4	0.35	0.088

Table V-6. Characterization of CdTe pillars before and after selective growth process.

V.6.B. Growth at 490°C

To avoid the adsorption of CdTe molecules between the CdTe pillars, the substrate temperature needs to be increased, and the CdTe flux is decreased to fit with the flux used in the study about nucleation on silicon. Accordingly, for this second selective growth attempt, the substrate temperature is set to 490°C (slightly above the highest nucleation temperature of 480°C) and exposed to a CdTe flux of $1.0 \cdot 10^{-7}$ mbar (measured on the flux gauge) for 2 hours. In-situ PEEM and ex-situ profilometry post-growth measurements are displayed in Figure V-26.

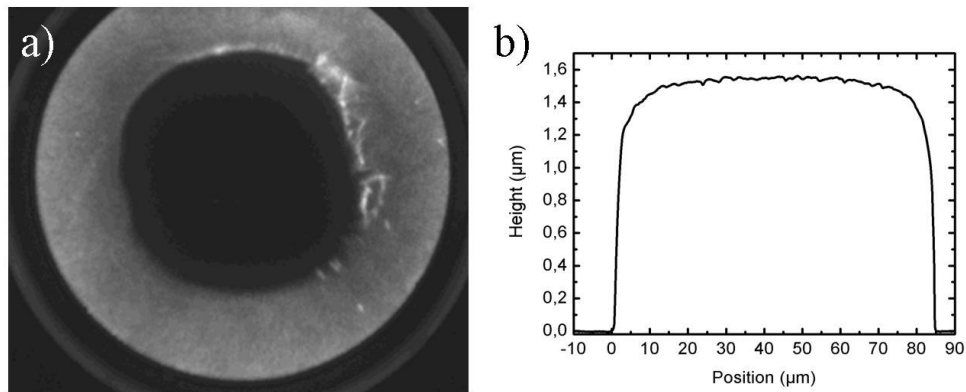


Figure V-26. Growth at 490°C: a) PEEM on CdTe pillar; b) Height of the pillar by profilometry.

Compared to the height of the reference sample, the height of the islands after the growth is increased to 1.53 μm , equivalent to a growth rate of 0.2 nm/s. This measurement of the

growth rate is in agreement with the grow rate vs temperature relation presented in Figure V-20 for the flux of $1.0 \cdot 10^{-7}$ mbar and a substrate temperature of 490°C .

No additional structures are observed by PEEM, so the conclusion is that the growth process is selective with these growth conditions. At this step, it is demonstrated that the selective growth by molecular beam epitaxy is possible for II-VI compounds [108, 109]. This new result extends the selective epitaxy process already demonstrated for III-V semiconductors by molecular beam epitaxy [110-112], metal-organic vapor phase epitaxy [113-115] and low pressure hydride vapor phase epitaxy [116].

V.7. Interferometric lithography

V.7.A. Interferometric lithography: fundamentals

The major problem of optical lithography occurs for the patterning of nanometer scale features. Diffraction of the UV beam occurs when the size of the feature is comparable or smaller than the wavelength of the UV light (typically 248 nm from a KrF excimer laser).

The minimum resolvable period (R) by optical lithography is defined as the ability to separate two patterns and can be estimated from Fresnel diffraction. It depends on the spacing between the mask and the substrate (g), the thickness and the refractive index of the photoresist (respectively d and n) and the wavelength of the illuminating UV light (λ) [117]:

$$R = 3 \sqrt{\frac{\lambda}{n} \left(g + \frac{d}{2} \right)} \quad (5.11)$$

Typical values for the optical lithography process used previously are $g = 1 \mu\text{m}$, $d = 1.8 \mu\text{m}$, $\lambda = 248 \text{ nm}$ and $n = 1.5$. The calculated resolution is $1.7 \mu\text{m}$. This basic calculation confirms that optical lithography is not suitable for the patterning of structures at the nanometer scale.

An alternative way to pattern small features is interferometric lithography (IL). It is a method to create periodic arrays without any mask, based on the interference between two coherent laser beams. Interference between two beams provides a periodic 1D pattern. Additional exposures with the sample rotated create the required pattern. The physics behind interferometric lithography is that a sinusoidal standing wave is produced with the

interference of the laser beams. Its spatial period (D) is a function of the wavelength (λ) and the angle θ between the wave vector and the surface normal (Figure V-27):

$$D = \frac{\lambda}{2 \sin \theta} \quad (5.12)$$

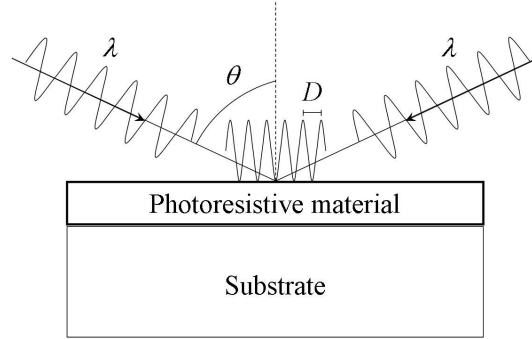


Figure V-27. Interferometric lithography.

The photoresist is burnt where the standing wave reaches a maximum whereas it is unchanged when the intensity is weak.

Because of the nanometer size of the expected pillars after using a developing solvent, dry etching is required for patterning the surface. Hence, the layer must be thin in order to enhance the etching accuracy.

V.7.B. Interferometric lithography on SOI

For this selective growth study, the substrate consists of silicon on insulator (SOI): 20 nm-thick Si(100) on 145 nm-thick SiO₂ layer grown on Si(100) provided by SOITEC (France).

SOI sample is etched in a piranha solution (H₂SO₄:H₂O₂ with a 5:1 ratio) for 10 minutes at 95°C and rinsed afterwards in DI water. A layer of antireflective coating (ARC) XHRI-16 is spin coated on the sample at 4000 rpm for 30 seconds and baked at 175°C for 3 minutes. A positive photoresistive material is then spin coated at 3000 rpm for 30 seconds and baked at 95°C for 1 minute. The sample is then exposed for 15 seconds to two IL process, rotated each other by 90°, creating a 2D pattern. The IL UV light consists of a 355 nm wavelength radiation (third harmonic of a YAG laser) with an incidence angle $\theta = 80^\circ$. The photoresist is developed in a MF702 developer for 75 seconds. The remaining photoresist pillars on the SOI substrate can be observed by SEM (Figure V-28a).

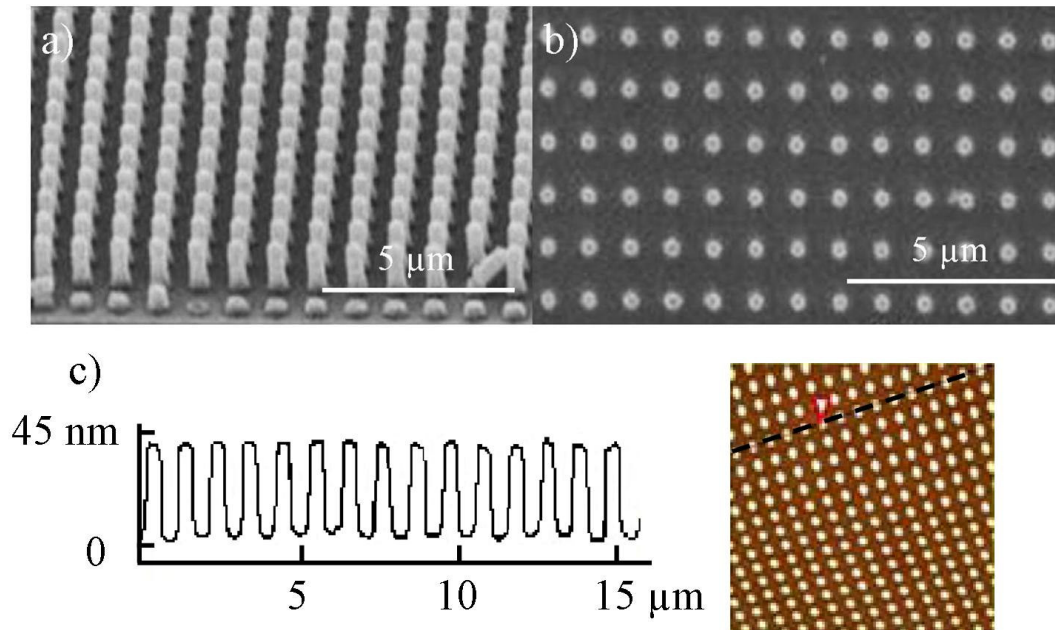


Figure V-28. SEM picture of a) photoresist pillars on SOI; b) Si pillars on SiO₂ after DRIE; c) AFM picture and line profiles of Si pillars on SiO₂.

Dry reactive ion etching (DRIE) with Ar, CHF₃ and O₂ gases as precursors was used to transfer the nanoscale patterns into the silicon layer. The etched sample is studied by SEM and atomic force microscopy (AFM) (Figure V-28b and c). The height and the width of the Si pillars are respectively 38 and 293 nm. The measured height is larger than the thin Si layer initially grown on the SiO₂. This means that the DRIE process also etches the SiO₂ and that the final structure consists of Si with a base composed of SiO₂ pillars which are patterned on SiO₂. The width of the pillars is measured to be on average 293 nm, with a mean height of 38 nm.

V.8. Selective growth on SiO₂ patterned substrate

In section V.6., the selective growth of CdTe on CdTe seeds on SiO₂ has been demonstrated. In this section, the selective growth of CdTe on Si(100) seeds on SiO₂ is studied. The experiment is carried out in the OPUS 45 MBE chamber.

Before the loading in the UHV environment, the patterned sample is subjected to an ex-situ chemical cleaning process involving a piranha clean for 5 minutes followed by a buffered oxide etch (NH₄F:HF:NH₄OH with a concentration ratio 21:3:1) for 10 seconds. At the end of the cleaning, the sample is rinsed in DI water for 5 minutes and blown dry with nitrogen.

Two samples (referenced hereafter as Reference sample and Selective growth sample) are chemically cleaned according to this procedure and are set on a molybdenum sample holder so that the back side can directly be exposed to the heating system by radiation and the front side can be exposed to the CdTe flux. Upon loading in the UHV environment, the samples are outgassed for 8 hours at 500°C before being transferred to the MBE chamber.

A multiple steps growth is performed to demonstrate the selective process:

- The sample is heated up to 1050°C for 1 minute to desorb the oxide on the top of the silicon pillars. The thick SiO₂ between the islands is not completely desorbed because no RHEED change is observed. During the cooling process from 1050°C to 400°C, the substrate is exposed to an As₄ flux to passivate the surface;
- A CdTe nucleation layer is grown for 5 minutes on the substrate kept at a temperature of 310°C, followed by the growth of a CdTe epilayer for 10 minutes at a temperature of 330°C ($p_{\text{CdTe}} = 2.0 \cdot 10^{-8}$ mbar). The Reference sample is transferred to atmosphere and studied by SEM showing that CdTe is grown all over the surface, both on Si pillars and on the SiO₂ between the islands;
- The CdTe is desorbed from the surface of the Selective growth sample kept in the UHV environment by heating the substrate up to 800°C for 10 minutes. Then the substrate is exposed to the same CdTe flux for 1 hour with the sample held at a temperature of 330°C (which is the highest nucleation temperature determined experimentally of CdTe on clean Si(100) for a CdTe flux of $2.0 \cdot 10^{-8}$ mbar. The value is obtained by the experimental procedure explained in V.4.B.). Because the bond between a metal and an oxide results from weak Van der Waals and chemical interactions [118], it is reasonable to assume that the highest nucleation temperature of CdTe on SiO₂ for the same flux is slightly lower.

The surface after the growth at 330°C is analyzed by SEM, X-ray photoelectron spectroscopy (XPS) and AFM (Figure V-29). It is obvious from the SEM picture that the diameter of the Si seeds is increased and nothing can be seen between the islands. This is confirmed by the XPS spectra: the Si 2p peaks are detected and they can be observed only if no CdTe is covering the SiO₂ surface between the pillars. From the SEM and XPS results, the conclusion is that the growth is selective and that with a CdTe flux of $2.0 \cdot 10^{-8}$ mbar and a substrate temperature of 330°C, the growth occurs only on the Si pillars, nothing growing on the SiO₂ between the islands.

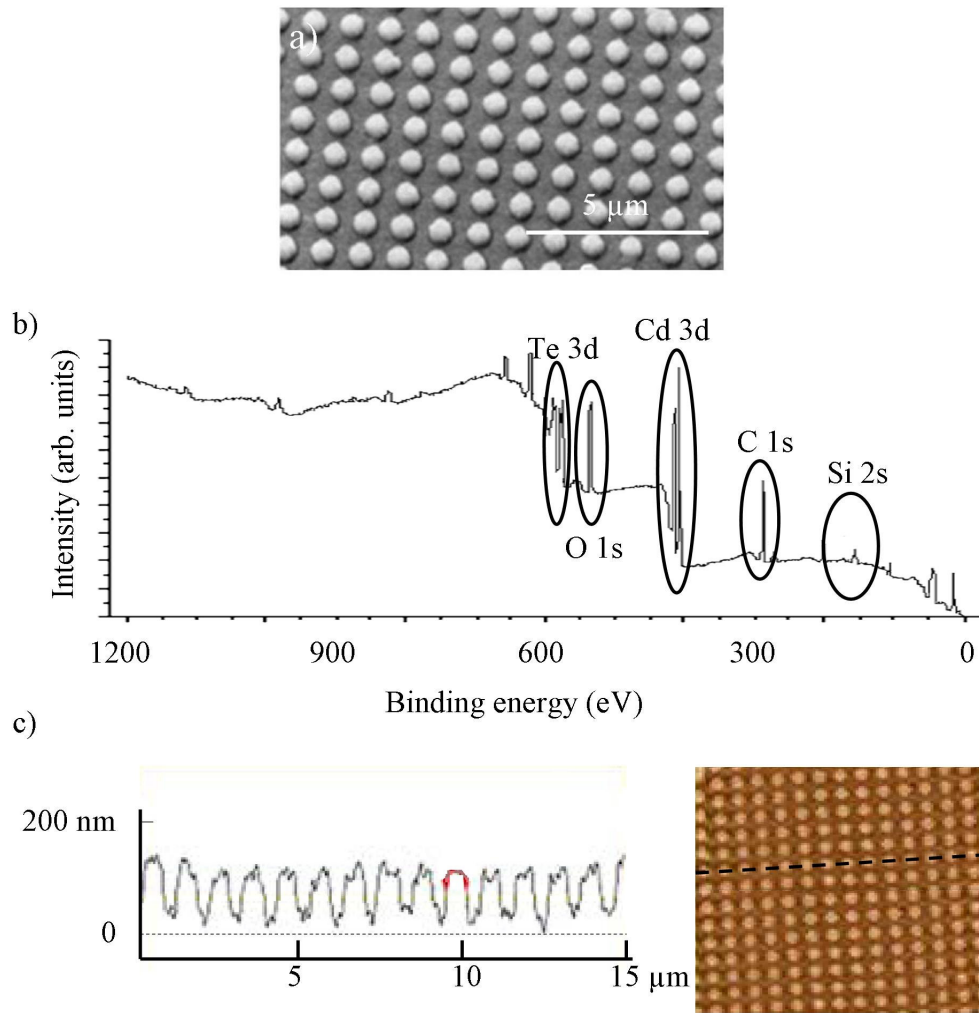


Figure V-29. CdTe selective growth on Si pillars on SiO₂: a) SEM picture; b) XPS spectra; c) AFM picture and line profile.

This conclusion is in contradiction with a previous work [119], but this is because the highest nucleation temperature difference of CdTe on Si and SiO₂ is probably very small.

Thanks to the AFM line profiles, it is possible to conclude that vertical and lateral growths occur during the selective process. The measured width and height of the pillars after the selective growth are respectively of about 615 nm and 95 nm compared to the previous equivalent values of 293 nm and 38 nm. The corresponding calculated lateral growth rate is about 0.45 Å/s and the vertical growth rate is 0.16 Å/s. For the vertical growth rate, the assumption is that the geometry of the tip is not a limitation of the height measurement because the remaining spacing between the islands (~300 nm) is large compared to the tip radius geometry. All the results on the IL patterned substrate are summarized in Table V-7.

	Before selective growth	After selective growth
Height	38 nm	95 nm
Pillar width	293 nm	615 nm
Vertical growth rate	0.016 nm/s	
Lateral growth rate	0.045 nm/s	

Table V-7. Selective growth of CdTe on Si(100) seeds patterned on SiO₂.

V.9. Selective growth mechanism

The selective growth process of CdTe is based on the difference in the maximum nucleation temperature of CdTe on different materials. Based on the growth rate versus temperature plot (Figure V-20), a mechanism is developed to explain this selectivity.

V.9.A. When an adatom lands on a surface...

When the adatom impinges on a surface, a wide variety of events can occur. It can be elastically scattered by the surface. It can also lose part of its energy by exciting vibrationally or electronically the atoms of the surface in its neighborhood. If this loss of energy is low, the adatom can then be inelastically reflected, but if this energy loss is sufficient, the adatom can be accommodated to the surface: the particle thermalizes at the substrate temperature T and is adsorbed on the surface. An adsorbed atom lies in a potential well which can be compared to the well-known Lennard-Jones potential defining the energy dependence of a diatomic molecule with respect to the interatomic distance. In the case of the interaction between an atom and a surface, the potential well may show two local minima (Figure V-30), one corresponding to a physisorbed state and one to a chemisorbed state:

- A physisorbed particle makes a weak Van der Waals bond with the substrate. This interaction involves no charge transfer and derives from the electrostatic attraction between the dipole moments from the adatom and from its nearest neighbors on the surface. The binding energy (E_{phys}) in this state is known to be inferior to 0.5 eV;
- If an exchange of electrons between the adatom and the substrate occurs, a chemisorbed state is created. The extreme case consists of the ionic bond where some valence electrons leave one atom to stay on the nearest neighbor. Most of the time, the exchange consists of a hybridization of the wavefunctions of the valence electrons of the substrate and the adsorbate to create a new wavefunction. The bonding electrons can then be seen as moving in the orbitals shared between the adatom and neighbors (covalent bond). The binding energy (E_{chim}) in this state ranges from 0.43 eV for nitrogen on nickel to 8.4 eV for oxygen on tungsten [120].

A potential barrier separates the chemisorbed and the physisorbed states. Depending on the height of this barrier, the lifetime of a physisorbed state is modified. Higher potential barriers result in longer lifetime. In order to be chemisorbed, the adatom has to cross a potential barrier with a height E_b . This can be done by receiving enough energy via electronic or vibrational processes or by tunneling effect.

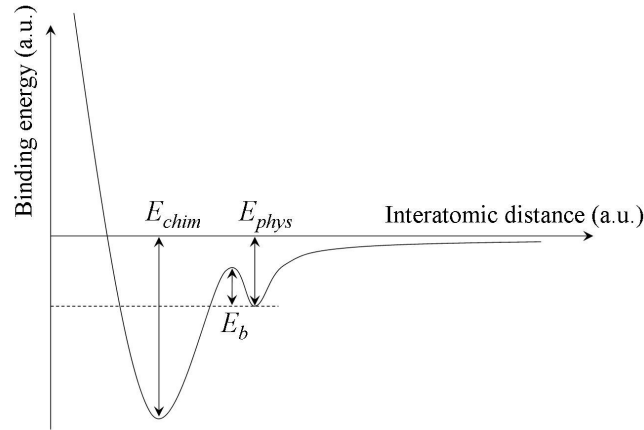


Figure V-30. Potential diagram for the adsorption process.

On a perfect surface (with no step and no defect), the maximum time of residence in a physisorbed or chemisorbed state (τ_{phys} and τ_{chim} respectively) before being desorbed from the surface is a function of the substrate temperature and the related energy:

$$\tau_{phys} = \tau_0 e^{\frac{E_{phys}}{kT}} \quad \text{and} \quad \tau_{chim} = \tau_0 e^{\frac{E_{chim}}{kT}} \quad (5.13)$$

In these equations, k is the Boltzmann constant and τ_0 is the inverse of the attempt frequency (ν_0) defined as the number of times per second that the adatom hits the barrier of the potential well. This frequency derives from the Heisenberg uncertainty principle and is equal to:

$$\nu_0 \approx \frac{kT}{h} \quad (5.14)$$

where h is the Planck's constant.

Although in the physisorbed or chemisorbed states, the adatoms can diffuse on the surface. It consists of the hopping from one atomic site to another (indicated by an arrow in Figure V-31) by thermal vibration or tunneling. On a perfectly flat surface, the energy required to hop is related to the potential barrier (W) separating two adjacent atomic sites. On an atomic step, the coordination of the atoms increases. Hence the surface potential (also called Ehrlich – Schwoebel potential W_{ES}) related to the step-edge increases. The numerical values of W and

W_{ES} given in the literature are mean values because of the defects on a real surface. Some of them are presented in Figure V-32: (1) perfectly flat surface, (2) a vacancy in the terrace, (3) a monoatomic step, (4) a vacancy in the ledge, (5) a step in the ledge (i.e. a kink), (6) an bulk-type adatom along the ledge, (7) another adatom on a terrace...

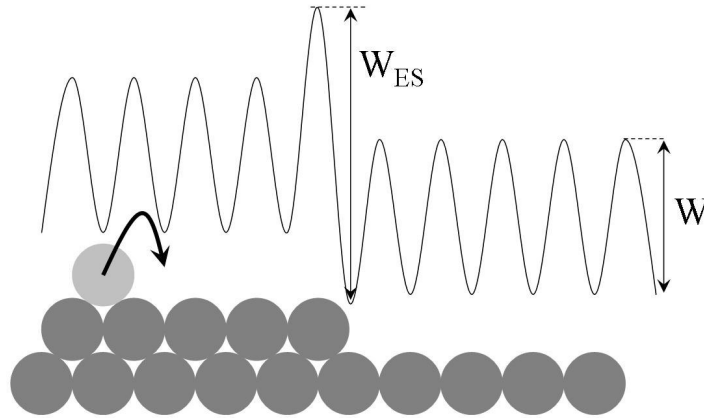


Figure V-31. Diffusion potential barriers on a terrace and at a step are denoted W and W_{ES} . The adatom and the substrate are represented in light and dark grey respectively.

On a terrace, the frequency ν at which the adatom will escape from one site to go to the next one depends on the barrier energy W and the number of closest neighboring sites (z):

$$\nu = z\nu_0 e^{-\frac{W}{kT}} \quad (5.15)$$

On an infinite flat surface, the adatom diffuses for a time τ_{diff} before being immobile:

$$\tau_{diff} = \tau_0 e^{\frac{E_{diff}}{kT}} \quad (5.16)$$

In the case of a vicinal surface such as the (211) orientation for example, the real average residence time can be very different from τ_{diff} (see section V.8.B.2. for a numerical application) because of the high density of steps acting as preferential nucleation sites.

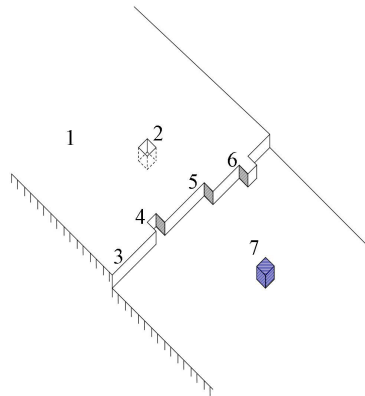


Figure V-32. Defects found on a surface (see text for legend).

Considering the residence time given by (5.13), the atomic desorption rate ($r_{d,i}$) from a chemisorbed or a physisorbed state can be seen as an Arrhenius process characterized by an energy E_{chim} and E_{phys} respectively and can be written as [121]:

$$r_{d,i} = Ae^{-\frac{E_i}{kT}} \quad (5.17)$$

In this equation, kT is the Boltzmann factor and A has to be experimentally determined. It is expressed in the same units as $r_{d,i}$ (ML/s or Å/s) and represents the frequency at which the proportion of atoms in a state i attempt to leave their binding state.

V.9.B. Modeling the CdTe growth rate

The growth rate of CdTe on a ZnTe buffer layer grown on Si(211) by MBE is reported in Figure V-20. During this experiment, the RHEED pattern changes immediately after exposure of the ZnTe surface to the CdTe flux. This reflects that a CdTe film is rapidly formed on ZnTe and that the deduced growth rates can be related to homoepitaxy of CdTe.

In the following, two different models are developed to interpret the growth rate curve. In all models, the growth rate (R) is expressed as a function of the incoming CdTe flux (F) and one or more Arrhenius desorption processes characterized by a desorption energy (E_{d1} and/or E_{d2}) and a pre-exponential term (a and/or b). The flux F represents only the impinging atoms which remain on the surface.

Desorption energy (eV)	CdTe orientation	Reference
1.92	(100)	[122]
1.54	(100)	[123]
1.95	(100)	[124]
1.98	(100)	[121]
1.9	(100)	[125]
2.21	(111)B	[123]
1.79	(111)A	[123]
1.92	Te ₂ from (111)B	[126]
1.13	Cd from (111)B	[126]

Table V-8. Desorption energies of CdTe from (100) and (111) surfaces.

Desorption of chemisorbed CdTe from (100) and (111) substrates has been extensively studied in the past. It is well established that CdTe desorbs in the form of Cd and Te₂.

Table V-8 presents the typical desorption energies given by the literature for (100) and (111) substrates.

Additionally, hybrid approach combining molecular dynamics and Monte Carlo simulations was used to estimate theoretically the energy of Cd-Cd, Te-Te, Cd-Te, Si-Te and Si-Cd chemical bonds [127]. These results are presented in Table V-9.

In the case of desorption from the physisorbed state, this binding energy is known to be inferior to 0.5 eV [128].

Chemical bond	Binding energy
Cd-Cd	0.58 eV
Te-Te	1.06 eV
Cd-Te	1.03 eV
Si-Te	1.22 eV
Si-Cd	0.88 eV

Table V-9. Binding energies of Cd-Cd, Te-Te and Cd-Te chemical bonds.

V.9.B.1. 1st model: one exponential term for the desorption

The first model considers only one component for the desorption process. This can be true if only one of the two existing states (physisorbed or chemisorbed) is largely predominant with respect to the other one. In this case, the growth rate follows an equation of the form:

$$R = F - a.e^{-\frac{E_d}{kT}} \quad (5.18)$$

The dashed curve in Figure V-33 represents this equation with the parameters F , a and E_d adjusted so that the model fits the experimental points. The mathematical relation is:

$$R(ML/s) = 1.9 - 2.5 \cdot 10^5 e^{-\frac{0.78eV}{kT}} \quad (5.19)$$

Although this function is characterized by a statistical R^2 calculation of 0.988 (i.e. a fitted curve highly representative of the experimental data), it is very difficult to explain the discrepancy with the literature data for the desorption energy and to find a physical interpretation of the pre-exponential term which should be related to the attempt frequency (between 10^{12} and 10^{13} Hz). Therefore, this model is rejected and the growth rate needs to be considered including at least 2 exponential terms.

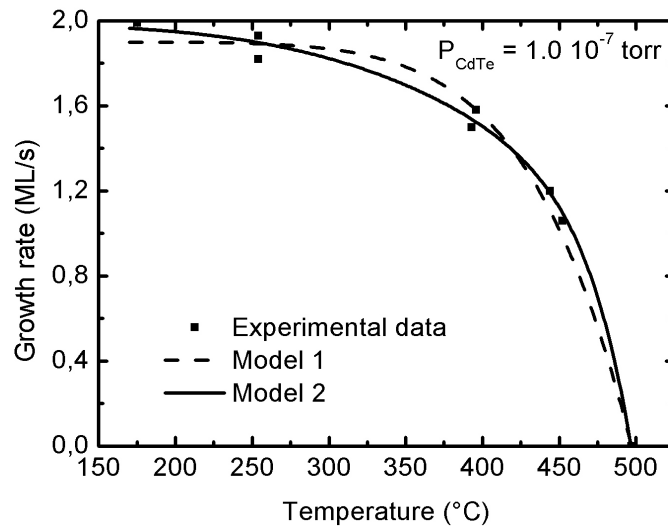


Figure V-33. Simulated models for the growth rate of CdTe on itself.

V.9.B.2. 2nd model: two exponential terms for the desorption

If the existence of both physisorbed and chemisorbed binding states are taken into account, a second model can be developed. The expression of the growth rate can then be written as:

$$R = F - a.e^{-\frac{E_{chim}}{kT}} - b.e^{-\frac{E_{phys}}{kT}} \quad (5.20)$$

Preliminary calculations need to be performed to evaluate the activation energy required for desorption from a chemisorbed state (E_{chim}). The calculation of E_{chim} is based on the lifetime of the different possible chemisorbed states compared to the diffusion time and the time interval between the arrivals of two adatoms of the same species.

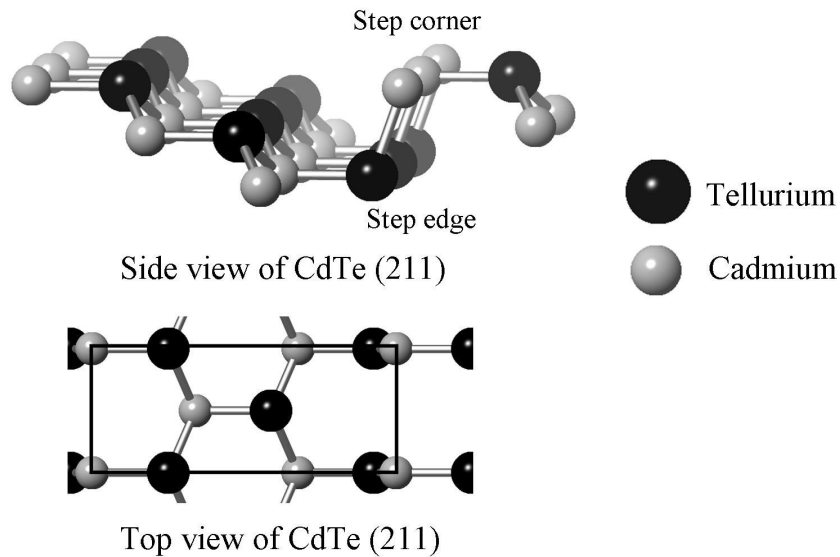


Figure V-34. Unit cell in a CdTe(211)B surface (rectangle).

The net impinging flux has been estimated around 2 ML/s when the CdTe flux corresponds to a read pressure of $1.0 \cdot 10^{-7}$ mbar. This means that the three Cd and three Te atoms needed per unit cell to form 1 ML arrive on a surface area of 52 \AA^2 (rectangle in Figure V-34) within 0.5 second. Hence the incoming time (per second and unit cell) for a Te or a Cd adatom ($\tau_{arrival}$) is given by:

$$\tau_{arrival} = 0.17s \quad (5.21)$$

In the case of the highly vicinal (211) surface, the growth is explained by a step flow process [129]: it is assumed that the adatom nucleates on a step where the dangling bond density is higher. Basic calculations can lead to an estimation of the time needed for an adatom to diffuse from the arriving point up to a step edge (τ_{diff}). The mean activation energy for surface diffusion for a chemisorbed Cd and Te atoms on a CdTe(100) surface is 0.9 eV [130]. For this particular orientation, diffusing atoms need to break two bonds for hopping from one site to the neighboring one. In case of the (211) surface, the atom arriving on a (111) terrace is singly bound before hopping up to a step edge [131]. Hence, one can expect the diffusion energy on the (111) terrace to be 0.45 eV. The area visited by the adatom per second is given by [132]:

$$D = D_0 e^{-\frac{E_{diff}}{kT}} \quad (5.22)$$

In this equation, we neglected the contribution of the entropy term because the atomic sites available for the hopping are all similar. For a surface with a 4-fold symmetry, the factor before the exponential is related to the attempt frequency (ν_0) and the distance between the adjacent atomic sites (a):

$$D_0 = \nu_0 a^2 \quad (5.23)$$

The time for diffusion to a step edge depends on the width of a (111) terrace (in our case: $d = 2a$). Hence considering that the visited area is a square, the time required to diffuse to a step edge is:

$$\tau_{diff} = \frac{d^2}{D} = \frac{4}{\nu_0} e^{\frac{E_{diff}}{kT}} \quad (5.24)$$

This function is presented in Figure V-35 as a function of the substrate temperature.

The time for the adatom to diffuse (τ_{diff}) from the adsorption site to the step corner or the step border (defined in Figure V-34) has to be compared to the time needed for the adatom to desorb from the chemisorbed state (τ_{chim}). From binding energies consideration, it is obvious that the first desorbing adatoms are the single bound ones. On a (111) terrace, an impinging

Te adatom can be singly bound to a Te atom of the terrace (binding energy of 1.06 eV) and a Cd adatom can be bound to a Te atom (with a binding energy of 1.03 eV). The life time of a singly bound adatom is expected to be:

$$\begin{aligned}\tau_{Te-Te} &= \tau_0 e^{\frac{1.06\text{eV}}{kT}} \text{ for Te adatom} \\ \tau_{Cd-Te} &= \tau_0 e^{\frac{1.03\text{eV}}{kT}} \text{ for Cd adatom}\end{aligned}\quad (5.25)$$

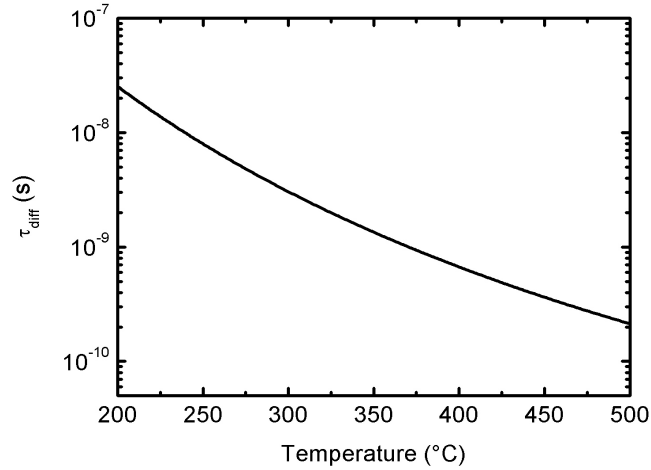


Figure V-35. Time of diffusion for $E_{diff} = 0.45$ eV.

These relations are plotted in Figure V-36. The dashed and solid curves are respectively for Cd and Te adatoms singly bound to a Te atom of the (111) terrace.

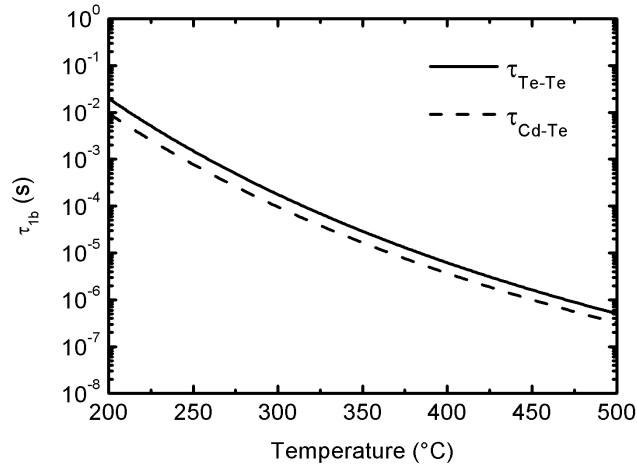


Figure V-36. Lifetime of singly bound adatoms on a (111) terrace.

These desorption times are longer than the time required for the adatom to diffuse up to a nucleation center situated at a step edge or step corner. Hence, one can suppose that the impinging adatom can directly make the following bonds:

- Te adatoms are singly bound with Te atoms of the terrace. If they arrive at a step corner, they make two bonds with two Cd atoms (yellow atom in Figure V-37). This chemisorbed state is characterized by a lifetime equal to:

$$\tau_{Te-2Cd} = \tau_0 e^{\frac{2.06eV}{kT}} \quad (5.26)$$

This time (represented by the black curve in Figure V-38) is long compared to the time before the arrival of a next Te adatom on the surface (see equation (5.21)), hence one can expect that the neighboring site at the step edge can be occupied by another Te adatom before the desorption of the first Te (this is important for the desorption process explained hereafter);

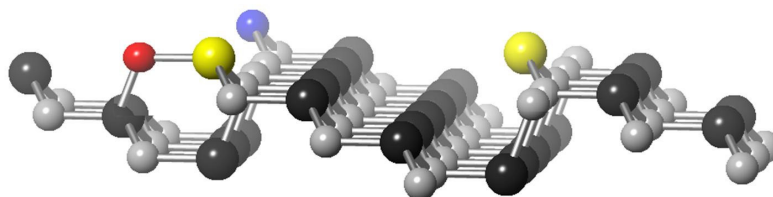


Figure V-37. Adatom diffusion and nucleation on a (211) surface.

- The Cd adatoms diffuse on the terrace, making one single bond with Te atoms. If a Te adatom is already nucleated at a step edge, the Cd adatom can create a second bond with this tellurium atom (red atom in Figure V-37). This configuration is stable and characterized by a residence time of (dashed curve in Figure V-38):

$$\tau_{Cd-2Te} = \tau_0 e^{\frac{2.06eV}{kT}} \quad (5.27)$$

In this case, the result is that the Te adatom at the step edge is triply bound to Cd atoms and the Cd adatom is doubly bound to Te atoms (this configuration is responsible for the step flow growth). The residence time of the Te adatom is drastically increased (solid curve in Figure V-38).

If no Te adatom is at the step edge, the Cd goes back up to a step edge of the terrace and nucleate with two Cd atoms (blue atom in Figure V-37). This process has a short lifetime compared to the time between the arrival of the next Cd atom on the surface. Hence single Cd atom must be taken into account for the desorption process (dotted curve in Figure V-38):

$$\tau_{Cd-2Cd} = \tau_0 e^{\frac{1.16eV}{kT}} \quad (5.28)$$

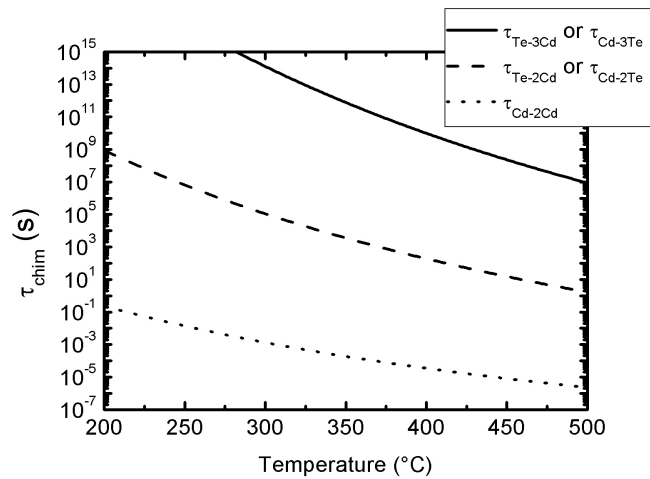


Figure V-38. Time before desorption from the chemisorbed state for different binding configurations.

The time scales involved in each chemisorbed state described before are very different. The limiting factors for the growth are: desorption of triply bound Te atoms at the step edge under the form of Te_2 or desorption of doubly bound Cd atoms at a step corner. In both cases, the residual atom (Cd singly bound in the first case and Te doubly bound in the second case) has a resulting lifetime much shorter than the arrival time of a stabilizing adatom and hence its desorption is considered to be unavoidable. The activation energy for this desorption process can be estimated, based on the theoretical binding values given in Table V-9:

- Considering the desorption of a triply bound Te atom, it is well known from literature [121, 131] that if the neighboring sites are occupied by Te atoms, Te desorbs under the form of Te_2 . Hence, the energy barrier to desorb one Te atom is not 3.09 eV (three bonds to be broken) but 2.03 eV for a Te_2 molecule (6 bonds broken – 2 bonds created for one Te_2 molecule), or half of that per Te atom;
- If the first atom to desorb is monoatomic Cd doubly bound to Te atoms, the energy required to break 2 bonds is estimated to be 2.06 eV.

The activation energy to desorb from a physisorbed state is extracted from the study of Behr *et al.* [133]. They modeled the growth rate of CdTe on CdTe(100) using both a chemisorbed and a physisorbed state to fit the experimental data. They obtained the following equation:

$$R = 1.57 - 4.0 \cdot 10^{15} e^{-\frac{1.89\text{eV}}{kT}} - 11.7 e^{-\frac{0.14\text{eV}}{kT}} \quad (5.29)$$

To simulate the growth curve obtained in our study concerning the growth rate of CdTe on CdTe(211)B, the same initial values for the prefactors a and b and for the activation energies (E_{phys} and E_{chim}) are inserted in the model before being adjusted by non-linear regression.

The equation obtained for the growth rate is represented by the solid line in Figure V-33 and given by:

$$R = 1.98 - 2.7 \cdot 10^{12} e^{-\frac{1.90\text{eV}}{kT}} - 194 e^{-\frac{0.35\text{eV}}{kT}} \quad (5.30)$$

This model corresponds to a physisorbed state characterized by a desorption energy of 0.35 eV and a chemisorbed state with a potential well depth of 1.90 eV. The R^2 of this non-linear regression makes it mathematically representative (0.995). Moreover, the energies and the prefactors of the model can be physically interpreted.

The lifetime of the physisorbed state is very short (because of the low activation energy for this process); hence one can deduce that the energy barrier between the physisorbed and the chemisorbed state is very low and that the physisorbed species are quickly chemisorbed. In other words, because of the lifetime associated to a physisorbed and a chemisorbed atom, the proportion of adatoms in the physisorbed state is much lower than the chemisorbed one.

An E_{chim} value of 1.90 eV is in agreement with the experiments carried out on CdTe(100) and CdTe(111) and is close to the energy calculated before, based on the binding energies and the number of bonds to be broken to desorb a Te atom. An E_{phys} value of 0.35 eV lies within the typical range (below 0.5 eV).

The prefactor a is related to the attempt frequency of a chemisorbed particle to leave its binding state and the proportion of chemisorbed species in 1 ML of adsorbed atoms. In the present case, this fraction is close to 1 (see below).

The prefactor (b) can be upper-bounded using basic calculations. From equation (5.17), the coefficient b is a function of the attempt frequency ν_0 for leaving this state and the fraction of adatoms in the physisorbed state N_{phys} . Hence, the desorption rate from the physisorbed state can be written as:

$$r_{phys} = b \cdot e^{-\frac{E_{phys}}{kT}} = \nu_0 N_{phys} \cdot e^{-\frac{E_{phys}}{kT}} \quad (5.31)$$

The fraction of one ML of adatoms in the physisorbed state N_{phys} can be roughly estimated: an impinging adatom is physisorbed for a time τ_b which depends on the potential barrier (E_b) separating the physisorbed and the chemisorbed state (Figure V-30). If the net flux of particles arriving on the surface F gives a constant growth rate and if the time required to cover the surface with 1 ML of adatoms (T) is higher than τ_b , then N_{phys} can be obtained as:

$$N_{phys} = \frac{\tau_b}{T} \quad (5.32)$$

The time T is derived from the impinging flux F :

$$T = F^{-1} \quad (5.33)$$

τ_b is not known, but it can be upper-bounded by the time required to desorb from the physisorbed state τ_{phys} , given by (5.13). So the value of the parameter b can be upper-bounded by:

$$b(ML/s) = v_0 N_{phys} = v_0 \tau_b F \leq v_0 \tau_{phys} F = F \cdot e^{-\frac{E_{phys}}{kT}} = 2e^{-\frac{0.35eV}{kT}} \quad (5.34)$$

This function is plotted in Figure V-39 and the value obtained by the non linear regression for b is in the acceptable range.

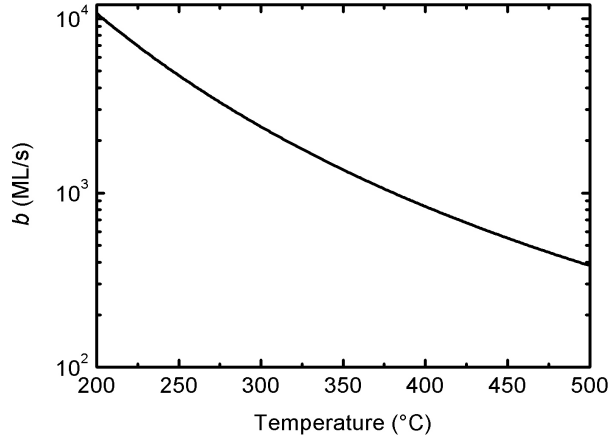


Figure V-39. Upper-bound for the desorption coefficient of the physisorbed state.

V.9.C. Selective growth of CdTe on CdTe seeds on SiO₂

This section is dedicated to the explanation of the selective growth observed on the CdTe sample patterned by optical lithography to create CdTe islands on Si. The Si substrate between the islands is naturally oxidized due to air exposure. We must know how to explain the fact that CdTe can grow on the pillars without sticking to the SiO₂ in between.

The selective growth process is detailed in Figure V-40: it is experimentally observed that for a given substrate temperature, no impinging atom remains on the substrate between the CdTe pillars. However, for the atoms arriving on the pillar, two events can occur. They can either diffuse on the pillar surface to nucleate at a step or they can desorb from a physisorbed or a chemisorbed state.

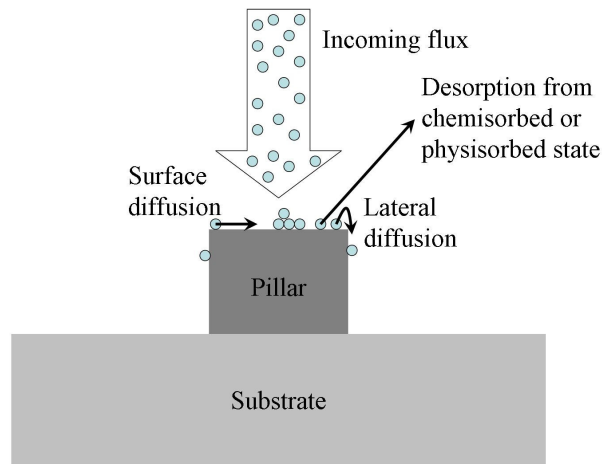


Figure V-40. Selective growth of CdTe on a pillar. Surface and lateral diffusions of atoms from an incoming flux are presented. Desorption from a physisorbed or a chemisorbed state can happen.

The growth rate curve modeled in the previous section represents the adsorption of CdTe molecules on a preexisting CdTe layer. The curve modeling the adsorption of CdTe on the SiO₂ substrate between the islands needs to be determined. This can only be done theoretically because upon the first CdTe layer is grown on SiO₂, the studied case is again the homoepitaxy of CdTe.

The idea is to keep a general expression similar to equation (5.30) in order to model the growth on SiO₂: the *a* prefactor is unchanged, the *b* parameter is adjusted to consider the different nature of the substrate, the net flux *F* is kept constant and the chemisorption and physisorption energies are dependent variables to be adjusted.

The upper-bond of the *b* factor (see equation (5.34)) depends on the activation energy to desorb from the physisorbed state.

Hence, the model for the growth of CdTe on SiO₂ can be modeled as:

$$R = 1.98 - 2.7 \cdot 10^{12} e^{-\frac{E_{chim}}{kT}} - 194 e^{-\frac{E_{phys}}{kT}} \quad (5.35)$$

To determine the E_{chim} and E_{phys} parameters, an additional consideration has to be taken into account: in Figure V-20, the blue line represents the highest substrate temperature at which nucleation of CdTe on silicon is observed within 2 minutes of exposure to the molecular flux. So these parameters are adjusted to obtain a growth rate of 0 ML/s at 480°C.

In Figure V-41, the equation (5.35) is drawn for several values of E_{phys} and E_{chim} . The solid curve represents the growth of CdTe on CdTe (via equation (5.30)).

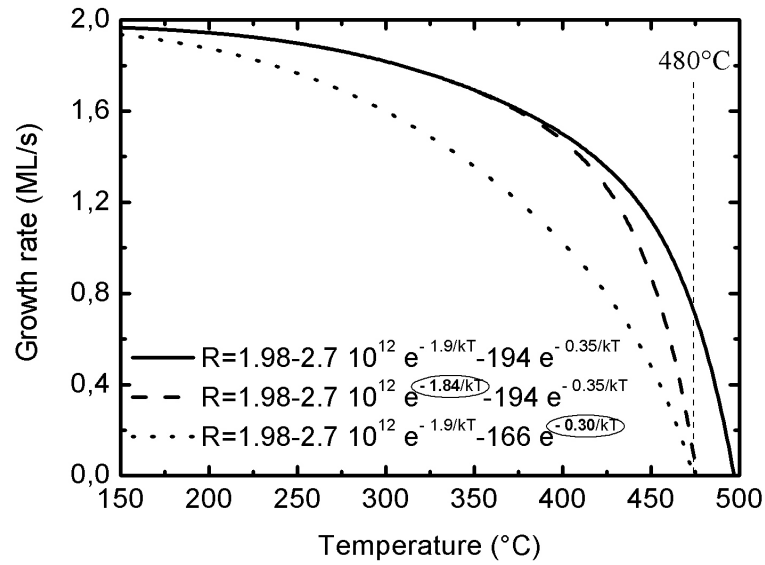


Figure V-41. Solid curve: CdTe growth on CdTe; Dashed curve: CdTe grown on SiO₂ with a different chemisorption energy; Dotted curve: CdTe grown on SiO₂ with a different physisorption energy.

The dashed curve simulates equation (5.35) with a physisorption energy unchanged compared to the growth of CdTe on CdTe ($E_{phys} = 0.35$ eV). Only the activation energy to desorb from the chemisorbed state is a variable. This curve is not physically convincing because the growth curves for CdTe on CdTe and CdTe on SiO₂ differ only if the substrate temperature is higher than 370°C whereas a difference in the growth rate is expected in the whole temperature range by modifying the chemisorption energy. The fact that the chemisorption energy remains constant should be verified by molecular dynamics calculations (not available) calculating the desorption energy of adatoms of Cd or Te on SiO₂.

The dotted curve corresponds to a change in the physisorption energy. By reducing the value of E_{phys} from 0.35 eV down to 0.30 eV, the growth rate of CdTe on SiO₂ is zero at a substrate temperature of 480°C. In addition, the prefactor of the physisorbed term is modified in the same proportion that E_{phys} to take into account the fact that the upper-bound of this prefactor is dependent on the physisorption energy (see (5.34)). Note that even if the prefactor b is kept constant, a physisorption energy of 0.31 eV is calculated to fit the experimental data. The variation in the physisorption energy can be explained by the ionic property of CdTe. Indeed, the Van der Waals forces result from the interaction of induced or permanent dipoles between

the adatom and the substrate. When a Cd or a Te atom arrives on a CdTe or a SiO₂ substrate, the interaction is stronger with the CdTe substrate because the electronic cloud is more deformed due to the higher Pauling's ionicity of CdTe (0.67) [134] compared to SiO₂ (0.45) [135].

In conclusion, the selective growth of CdTe on CdTe compared to SiO₂ is explained by the difference in the physisorption of the adatom. The bond is weaker between Cd and SiO₂, so the atoms arriving on the SiO₂ substrate desorb from the physisorbed state before being chemisorbed with the substrate.

The equations governing the growth of CdTe on CdTe and SiO₂ are respectively:

$$\begin{aligned} R_{CdTe} &= 1.98 - 2.7 \cdot 10^{12} e^{-\frac{1.90eV}{kT}} - 194 e^{-\frac{0.35eV}{kT}} \\ R_{SiO_2} &= 1.98 - 2.7 \cdot 10^{12} e^{-\frac{1.90eV}{kT}} - 166 e^{-\frac{0.30eV}{kT}} \end{aligned} \quad (5.36)$$

V.9.D. Selective growth of CdTe on Si(100) seeds on SiO₂

The second experiment on selective growth deals with the growth of CdTe on Si(100) pillars patterned on SiO₂. For this experiment, the CdTe flux is $2.0 \cdot 10^{-8}$ mbar. The consequence is that the net flux F determined for a CdTe flux of $1.0 \cdot 10^{-7}$ mbar has to be modified to take into account the flux variation. The growth rate equation of CdTe on SiO₂ between the islands (see equation (5.36)) can then be written as:

$$R_{SiO_2} = 0.40 - 2.7 \cdot 10^{12} e^{-\frac{1.90eV}{kT}} - 166 e^{-\frac{0.30eV}{kT}} \quad (5.37)$$

From the experiment, the highest nucleation temperatures of CdTe on SiO₂ and Si(100) were respectively 310°C and 330°C. If the equation (5.37) is plotted in Figure V-42, the growth rate on SiO₂ (dashed curve) equals 0 for a substrate temperature of 303°C (instead of 310°C experimentally). This incoherence can be explained by the fact that the MBE systems used for the selective growth of CdTe on CdTe seeds and on Si(100) seeds are different. Hence, the temperature calibration and the flux measurement can be slightly different. Nevertheless, the temperature difference between the highest nucleation temperatures needs to be constant. Hence, the growth rate on Si is modeled so that the growth rate equals 0 when the substrate temperature is 323°C (solid curve in Figure V-42). This result is achieved when E_{phys} is set to 0.31 eV. The chemisorption energy is kept constant because the energy required to brake two binding bonds is in the same range that the chemisorption energy theoretically calculated for

the previous case. Hence, the slight difference between the physisorption of Cd or Te adatoms on Si and SiO₂ can explain that in the adequate temperature window CdTe can grow on Si without growing on SiO₂.

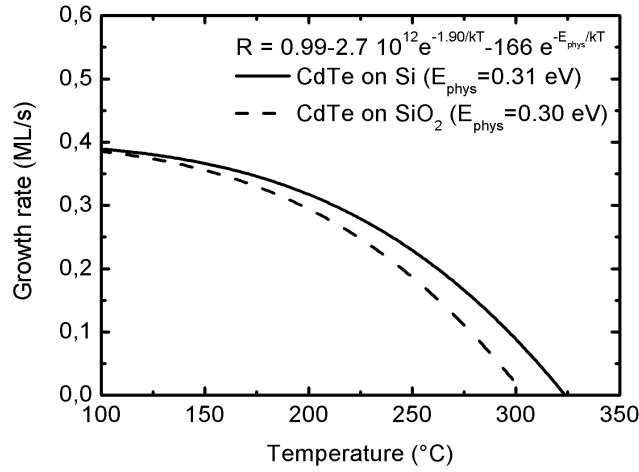


Figure V-42. Growth rate of CdTe on SiO₂ (dashed curve) and Si (solid curve).

In summary, for the growth of CdTe on Si pillars patterned on SiO₂, the selective growth process is possible because of different physisorption energies and the related growth rates are respectively:

$$R_{\text{SiO}_2} = 0.40 - 2.7 \cdot 10^{12} e^{-\frac{1.90\text{eV}}{kT}} - 166 e^{-\frac{0.30\text{eV}}{kT}} \quad (5.38)$$

$$R_{\text{Si}} = 0.40 - 2.7 \cdot 10^{12} e^{-\frac{1.90\text{eV}}{kT}} - 166 e^{-\frac{0.31\text{eV}}{kT}}$$

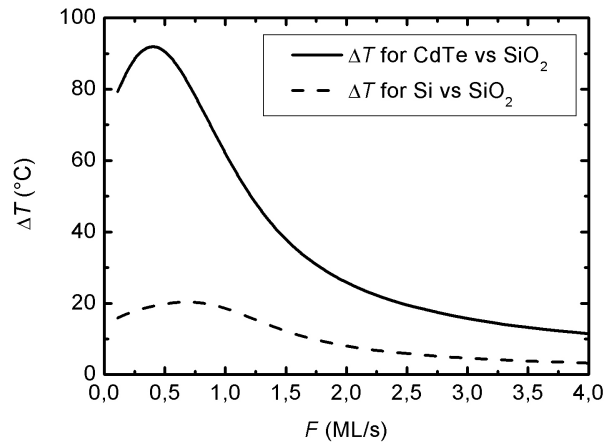


Figure V-43. Difference in the nucleation temperatures as a function of the incident flux F .

This very small difference in the physisorption energy explains that selective growth of CdTe on Si vs SiO₂ was not reported in a previous study [119]. Indeed, depending on the initial net flux F and using equation (5.38), the difference (ΔT) between the highest nucleation

temperature on Si and SiO₂ or CdTe and SiO₂ can be simulated by a FORTRAN program. The result is given in Figure V-43 and it is obvious that the flux has a strong influence on the temperature window to observe a selective growth process. The selective growth can easily be achieved with CdTe seeds on SiO₂ (solid curve), but the choice of the flux F is more critical for the Si seeds on SiO₂ system (dashed curve). In the latter case, the nucleation temperature difference rapidly tends to zero when the flux increases.

